

AD \_\_\_\_\_

GRANT NUMBER DAMD17-94-J-4058

TITLE: Development of a High Resolution Digital Mammography System

PRINCIPAL INVESTIGATOR: James K. Walker, Ph.D.  
Zhenxue Jing, M.S.

CONTRACTING ORGANIZATION: University of Florida  
Gainesville, Florida 32610-0226

REPORT DATE: December 1996

TYPE OF REPORT: Final

PREPARED FOR: Commander  
U.S. Army Medical Research and Materiel Command  
Fort Detrick, Frederick, Maryland 21702-5012

DISTRIBUTION STATEMENT: Approved for public release;  
distribution unlimited

The views, opinions and/or findings contained in this report are those of the author(s) and should not be construed as an official Department of the Army position, policy or decision unless so designated by other documentation.

19970421 035

# REPORT DOCUMENTATION PAGE

Form Approved  
OMB No. 0704-0188

Public reporting burden for this collection of information is estimated to average 1 hour per response, including the time for reviewing instructions, searching existing data sources, gathering and maintaining the data needed, and completing and reviewing the collection of information. Send comments regarding this burden estimate or any other aspect of this collection of information, including suggestions for reducing this burden, to Washington Headquarters Services, Directorate for Information Operations and Reports, 1215 Jefferson Davis Highway, Suite 1204, Arlington, VA 22202-4302, and to the Office of Management and Budget, Paperwork Reduction Project (0704-0188), Washington, DC 20503.

1. AGENCY USE ONLY (Leave blank)	2. REPORT DATE	3. REPORT TYPE AND DATES COVERED	
	December 1996	Final (15 Aug 94 - 14 Nov 96)	
4. TITLE AND SUBTITLE Development of a High Resolution Digital Mammography System			5. FUNDING NUMBERS DAMD17-94-J-4058
6. AUTHOR(S) James K. Walker, Ph.D. Zhenxue Jing, MS			
7. PERFORMING ORGANIZATION NAME(S) AND ADDRESS(ES) University of Florida Gainesville, Florida 32610-0226			8. PERFORMING ORGANIZATION REPORT NUMBER
9. SPONSORING/MONITORING AGENCY NAME(S) AND ADDRESS(ES) Commander U.S. Army Medical Research and Materiel Command Fort Detrick, Frederick, MD 21702-5012			10. SPONSORING/MONITORING AGENCY REPORT NUMBER
11. SUPPLEMENTARY NOTES			
12a. DISTRIBUTION / AVAILABILITY STATEMENT Approved for public release; distribution unlimited		12b. DISTRIBUTION CODE	
13. ABSTRACT (Maximum 200)  We have (1) investigated the effect of scattered radiation in a slot x-ray detector. The results enable the optimization of any scanning slot mammography system. (2) studied the variables that affect image quality of a plastic scintillating fiber screen (SFS). The effects of loading High Z element into SFS were investigated. Choice of a high Z element and its optimal concentration were determined. (3) made three key advancements over current plastic scintillating fiber technology: Improved plastic scintillating fiber energy conversion efficiency from ~3% to > 4.5%; Increased the scintillation light collection efficiency from 3% to 7.5%; Loaded up to 20% by weight of tin into plastic scintillator which remained a thermoplastic from which scintillating fibers were able to be produced. (4) developed a testing system to measure the imaging performance of a scanning slot x-ray detector. A circuitry for CCD dark current and detector non-uniformity corrections has been integrated into the CCD readout electronics. A measured total electronic noise level of 75 e <sup>-</sup> rms has been achieved at 2 MHz readout rate (per CCD) and 28°C. At this stage, intensive efforts are being taken to produce tin loaded scintillating fibers which are transparent to its scintillation light.			
14. SUBJECT TERMS Breast Cancer			15. NUMBER OF PAGES 47
			16. PRICE CODE
17. SECURITY CLASSIFICATION OF REPORT Unclassified	18. SECURITY CLASSIFICATION OF THIS PAGE Unclassified	19. SECURITY CLASSIFICATION OF ABSTRACT Unclassified	20. LIMITATION OF ABSTRACT Unlimited

FOREWORD

Opinions, interpretations, conclusions and recommendations are those of the author and are not necessarily endorsed by the U.S. Army.

Where copyrighted material is quoted, permission has been obtained to use such material.

Where material from documents designated for limited distribution is quoted, permission has been obtained to use the material.

Citations of commercial organizations and trade names in this report do not constitute an official Department of Army endorsement or approval of the products or services of these organizations.

In conducting research using animals, the investigator(s) adhered to the "Guide for the Care and Use of Laboratory Animals," prepared by the Committee on Care and use of Laboratory Animals of the Institute of Laboratory Resources, National Research Council (NIH Publication No. 86-23, Revised 1985).

For the protection of human subjects, the investigator(s) adhered to policies of applicable Federal Law 45 CFR 46.

In conducting research utilizing recombinant DNA technology, the investigator(s) adhered to current guidelines promulgated by the National Institutes of Health.

In the conduct of research utilizing recombinant DNA, the investigator(s) adhered to the NIH Guidelines for Research Involving Recombinant DNA Molecules.

In the conduct of research involving hazardous organisms, the investigator(s) adhered to the CDC-NIH Guide for Biosafety in Microbiological and Biomedical Laboratories.

 12-6-96  
PI - Signature Date

## TABLE OF CONTENTS

<b>INTRODUCTION</b>	5
Background	5
Current approaches to digital	5
Purpose of the research	6
Reference	6
<b>BODY</b>	8
<b>I. Computation of Scattered Radiation in Scanning Slot Digital Mammography</b>	8
I.1. Introduction	8
I.2. Method	8
I.3. Results	10
I.4. Discussion	14
I.5. Conclusion	16
I.6. References	16
<b>II. Investigation of Imaging Characteristics of the Plastic Scintillating Fiber Screens</b>	19
II.1 Introduction	19
II.2. Theory	19
II.3. Scintillating Fiber Screens	20
II.4. Monte Carlo Simulations	23
II.5. Selection of a High Z Element Loaded SFS	24
II.6. Optimization of the Tin Loaded Plastic Scintillating Fiber Screens	29
II.7. Reference	33
<b>III. Development of A Scanning Slot Digital X-ray Detector for Mammography</b>	35
III.1. Introduction	35
III.2. A scintillating fiber screen based slot x-ray detector	35
III.3. CCD Camera and Readout Electronics	38
III.4. A Prototype Testing System	39
III.5. Evaluation of a Prototype CsI:Tl Screen Based Slot X-ray Detector	42
III.6. A CsI:Tl Screen Based Slot X-ray Detector as an Alternative to the SFS based Slot X-ray Detector	44
<b>CONCLUSIONS</b>	45
<b>APPENDIX</b>	47
List of Publications	47
List of Personnel Receiving Pay	47

## INTRODUCTION

### Background

In the absence of any means to prevent the breast cancers, it is critical to detect the breast cancers at their early stages when they may be curable. Although screen-film mammography is the most reliable means of detecting nonpalpable breast cancers [1-3], there are four technical limitations which reduce its effectiveness: (1) Compromise between film contrast and latitude [4]; (2) film granularity significantly reduces the image signal-to-noise ratio at high spatial frequencies [5,6]; (3) Scatter rejection using grids leads to a factor of ~2 increase in mean glandular dose [7-11]; (4) Compromise between spatial resolution and absorption efficiency [5]. In practice, about 10 to 20% of breast cancers are mis-diagnosed due to the subtlety of the lesion and the limitation of image quality.

Digital mammography has the potential to overcome the limitations of screen-film mammography and to improve the sensitivity and specificity of breast cancer detection. The decoupling of image acquisition, storage, and display stages allows the optimization of each stage. Digital mammography also provides additional benefits including digital archive, computed assisted diagnosis and teleradiology.

### Current approaches to digital mammography

To realize the benefits of digital mammography, an x-ray imaging detector with appropriate characteristics must be developed. A recent ROC study [12] demonstrated that very high spatial resolution (a pixel size of 35 mm or smaller) will be required for digital mammography in order to capture the very subtle microcalcifications. It has also been shown that a digital mammography system should have a linear dynamic range over 400:1 [13,14]. The signal-to-noise ratio and contrast performance of the imaging system must be excellent to image the extremely subtle differences between tumor and normal breast tissue [15].

Various configurations for the acquisition of digital mammograms have been proposed [16-22]. The most attractive approach to digital mammography may be the use of the scanning slot x-ray detectors, which have the advantage of efficient scatter rejection without significant increase in breast glandular dose [23].

At present, several x-ray detection materials are being investigated for use in the scanning slot x-ray detectors. The initial slot x-ray detector design utilized a rare-earth phosphor slot screen (Gd<sub>2</sub>O<sub>2</sub>S:Tb) coupled by tapered fiber optic image guide to CCDs, which are operated in the time-delayed integration (TDI) mode [17,18]. There are intrinsic limitations of this design which mainly stem from the use of phosphor. (1) Using a phosphor coupled to a CCD via a fiber optic image guide will inevitably reduce the spatial resolution compared to modern screen-film mammography, for which a single emulsion film is used in combination with a single back-intensifying screen. (2) The afterglow (slow

scintillation decaying component) nature of Gd<sub>2</sub>O<sub>2</sub>S:Tb phosphor will likely prevent its use for fast scanning applications [24].

Another slot detector approach was to use a hybrid photodiode array which directly converts the x-rays into electrons[25]. It has the potential to provide high signal-to-noise performance. However, the noise from dark current generation as a result of large silicon volume, the radiation damage to the detector, and possible high detector cost will affect the use of the photodiode for scanning slot digital mammography.

It is necessary to investigate the other x-ray detection materials which have the appropriate imaging characteristics for application to scanning slot digital mammography.

### Purpose of the research

The primary goal of this predoctoral fellowship research project is to investigate the use of a plastic scintillating fiber screen (SFS) as the x-ray-to-light conversion material in a scanning slot x-ray imaging detector for mammography. Methods to maximize the scintillation light generation and output from an SFS will be developed. An SFS with optimized imaging performance will be constructed. A prototype scanning slot digital mammography detector based on the optimized SFS will be constructed, and its imaging performance will be evaluated.

### Reference

1. Zhou and R. Gordon, "Detection of Early Breast Cancer: An Overview and Future Prospects", Clinical Rev. in Biomedical Eng., Vol. 17, Issue 3, 203-255 (1989).
2. M. J. Yaffe, "Digital Mammography", Syllabus: *A Categorical Course in Physics Technical Aspects of Breast Imaging* Ed. by A.G. Haus and M.J. Yaffe, RSNA Publications, Oakbrook, IL, 245-255 (1992)
3. A.G. Haus, "Recent Advances in Screen-Film Mammography", Radiologic Clinics of North America, Vo. 25, No. 5, 913-927 (1987)
4. R. M. Nishikawa G. E. Mawdsley, A. Fenster and M. J. Yaffe, "Scanned-projection digital mammography", Med. Phys. 14, 5, 717-727 (1987).
5. Kuhn and W. Knupfer, "Imaging characteristics of different mammographic screens," Med. Phys. 19 (2) 449-457 (1992)
6. M. Nishikawa and M. J. Yaffe, "Signal-to-noise properties of mammographic film-screen systems", Med. Phys. 12(1), 32-39 (1985)
7. G.T. Barnes, I. A. Brezovich "The intensity of scattered radiation in mammography", Radiology 126, 1978, 243-247
8. G.R. Hammerstein, D.W. Miller, D.R. White, M.E. Masterson, H.Q. Woodard, J.S. Laughlin, "Absorbed Radiation Dose in Mammography", Radiology, 130: 485-491 (1979)
9. W. Huda, A.M. Sourkes, J.A. Bews, R. Kowaluk, "Radiation Doses Due to Breast Imaging in Manitoba: 1978-1988", Radiology 1990; 177: 813-816

10. R. Dance, J. Persliliden, G. A. Carlsson "Calculation of dose and contrast for two mammographic grids", *Phys. Med. Biol.*, 1992, Vol. 37, No. 1, 235-248
11. Gary T. Barnes, "Mammography Equipment: Compression, Scatter Control, and Automatic Exposure Control", Syllabus: *A Categorical Course in Physics Technical Aspects of Breast Imaging* Ed. by A.G. Haus and M.J. Yaffe, RSNA Publications, Oakbrook, IL, 59-68 (1992)
12. H. Chan, L.T. Niklason, D.M. Ikeda, K.L. Lam, "Digitization requirements in mammography: Effects on computer-aided detection of microcalcifications", *Med. Phys* 21(7), 1203-1211 (1994)
13. Gambaccini, M. Marziani, O. Rimondi "Phantoms and dynamic range in mammography", *Radiation Protection Dosimetry*, Vol. 49, Nos 1/3, pp 187-191 (1993)
14. Maidment, R. Fahrig, M. J. Yaffe "Dynamic range requirement in digital mammography", *Med. Phys.*, 20(6), Nov/Dec, 1993, 1621-1633.
15. P. C. Johns, M. J. Yaffe, "X-ray characterisation of normal and neoplastic breast tissues", *Phys. Med. Biol.*, 1987, Vol. 32, No. 6, 675-695
16. M. Nishikawa G. E. Mawdsley, A. Fenster and M. J. Yaffe, "Scanned-projection digital mammography", *Med. Phys.* 14, 5, 717-727 (1987).
17. A.D.A. Maidment, M.J. Yaffe, D.B. Plewes, G.M. Mawdsley, I.C. Soutar, B.G. Starkoski, "Imaging performance of a prototype scanned-slot digital mammography system", *Proc. SPIE* 1896, 93-103 (1993)
18. Piccaro and E. Toker, "Development and evaluation of a CCD-based digital imaging system for mammography", in *Electronic Imaging*. SPIE X (Feb. 1993)
19. A. Karellas, L.J. Harris, "Charge-coupled device detector: Performance considerations and potential for small-field mammographic imaging applications", *Med. phys.*, 19(4), 1015-23 (1992)
20. R. Fahrig, J.A. Rowlands, M.J. Yaffe, "X-ray imaging with amorphous selenium: Detective quantum efficiency of photoconductive receptors for digital mammography", *Med. Phys.* 22(2), 153-160 (1995)
21. U. Neitzel, I. Maack, SG Kohfahl, "Image quality of a digital chest radiography system based on a selenium detector", *Med. phys.*, 21(4), 509-16 (1994)
22. HG Chotas, CE Floyd, Jr, CE Ravin, "Technical Evaluation of a Digital Chest Radiography System That Uses a Selenium Detector", *Radiology* 1995; 195:264-270.
23. Z. Jing, W. Huda, J. K. Walker, "Scattered Radiation in Scanning Slot Mammography," Presented at *1995 RSNA annual meeting*, Nov., 1995, Chicago, *Radiology* Vol. 197(P), 1995, p221. Submitted to *Medical Physics* for publication.
24. Gluer, W.R. Dix, W. Graeff, W. Kupper and K.H. Stellmaschek, "A fast low-noise line scan x-ray detector," *Med. Phys.* 16(1), pp 98-104 (1989)
25. JM Henry, MJ Yaffe, Bo Pi, J. Venzon, F. Augustine, TO Tumer, "Solid state x-ray detectors for digital mammography," *SPIE* Vol. 2432, 392-401, 1995.

## BODY

### **I. Computation of Scattered Radiation in Scanning Slot Digital Mammography**

#### **I.1. Introduction**

In mammography, the production of scattered photons by the breast degrades subject contrast and inhibits the detection of low contrast features including subtle masses and microcalcifications. The amount of scattered radiation present may be quantified using the scatter to primary ratio (S/P) [1]. Major factors which affect the S/P ratio in screen-film mammography include the x-ray field size, x-ray photon energies as well as the breast thickness [1-3]. For screen-film mammography, S/P ratios can range from ~0.25 to ~1.2 with corresponding reductions in subject contrast of up to 50%. Grids with either 4:1 or 5:1 ratios, and strip line densities of between 30 and 50 per centimeter, can be used to minimize the amount of scatter incident on the mammography screen-film combination. As a result, the S/P ratio in screen-film mammography may be reduced to between ~0.10 and ~0.30 [4]. The use of grids, however, requires an increase in x-ray tube output which results in increased mean glandular doses by a factor of about two [5-7].

Imaging systems using a scanning slot detector geometry have been evaluated for use in digital mammography [8-11]. These designs use a collimated fan beam of x-rays with the slot detector moved to cover the whole breast region in about 4 to 6 seconds. The choice of slot detector width has typically ranged from ~4 mm to ~10 mm. Use of a smaller slot detector width will be expected to reduce the amount of scatter reaching the detector but will increase the x-ray tube loading [8]. Increasing the slot detector width permits the x-ray tube output to be more efficiently utilized and will enable the use of a shorter imaging time thereby reducing patient discomfort [12]. The size of the slot detector width directly affects the expected value of the S/P ratios with a value of ~0.1 reported by Fahrig *et al* [13] and a similar value of < 0.15 by Feig *et al* [14]. Specially designed grids used in conjunction with a scanning slot x-ray detector have been shown to result in large reductions in the S/P ratio, but at the price of an increase in radiation dose [13]. The amount of scattered radiation present in the scanning slot mammography systems, however, have not been systematically studied. Furthermore, scatter rejection by the use of air gaps also merits examination [15].

In this study, we performed Monte Carlo simulations to calculate the S/P ratios for a slot x-ray detector geometry using the x-ray photon energies currently used in screen-film mammography. The relative contributions of Compton and coherent scattering to the total scattered radiation reaching the detector were determined. The dependence of the S/P ratio on the slot detector material was examined. In addition, the scatter reduction by the use of an air gap was assessed and compared to that of using grids in conventional screen-film mammography.

#### **I.2. Method**

### Monte Carlo Simulation

The EGS4 Monte Carlo code [16] was employed to simulate the x-ray interaction processes in a Lucite phantom and the slot x-ray detector. The atomic electron binding effect on Compton scattering was taken into account by incorporating the changes in the EGS4 code reported by Namito *et al* [17]. The effect of molecular structure on coherent scattering in the Lucite breast phantom was included using methods described by Leliveld *et al* [18].

Monte Carlo simulations were performed using monoenergetic x-ray photons with energies ranging from 15 to 50 keV and for a representative mammographic x-ray energy spectrum taken from the measured data of Fewell and Shuping [19]. The x-ray spectrum was generated using a Mo target, an x-ray tube potential of 30 kV and with 30  $\mu$ m Mo added filtration. The x-ray spectrum is shown in Figure I.1 and has an average photon energy of 18.4 keV.

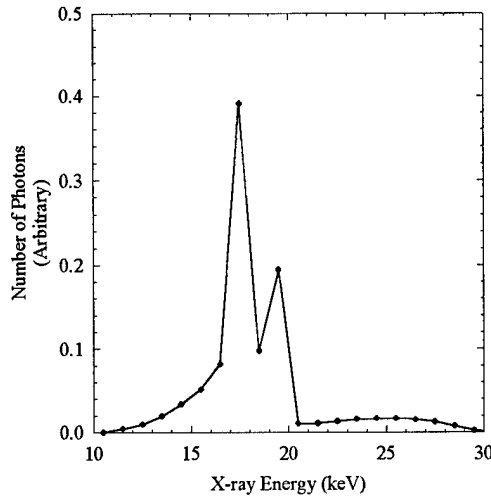


Figure I.1. A 30 kV mammography x-ray spectrum (Mo-anode, 30  $\mu$ m Mo filtration).

### Simulation Model

Figure I.2 shows the geometry used in the Monte Carlo simulations. The fan beam originates at a point focus and is collimated to the cross-sectional area of the slot detector. The breast was modeled by a homogeneous block of Lucite (20 cm x 20 cm cross sectional area) of thickness  $T$  which ranged from 2 to 6 cm. The x-ray source, one edge of the Lucite phantom, and one edge in the short dimension of the slot detector area were aligned at the chest wall as shown in Figure I.2. The slot detector was aligned with the center of the Lucite phantom with an x-ray source to detector distance of 60 cm. The length of the slot x-ray detector was 20 cm and the slot detector width,  $W$ , ranged from 4 mm to 20 mm. Unless otherwise specified, the Monte Carlo simulations had no air gap.

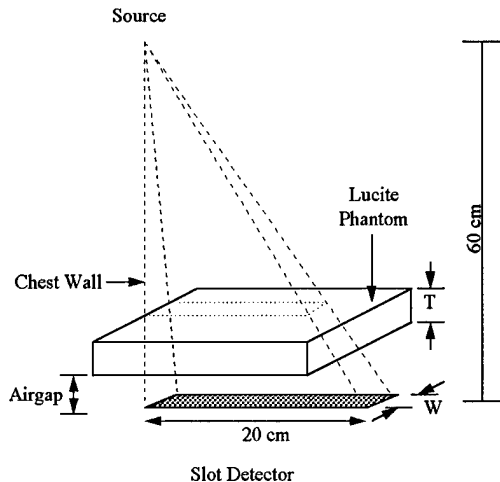


Figure I.2. Imaging geometry used in the Monte Carlo simulations.

Two slot x-ray detectors were studied. The first detector (Detector 1) was assumed to have a 100% efficiency for absorbing x-ray photons, regardless of their energies and angles of incidence. The second detector (Detector 2) consisted of a 50  $\mu\text{m}$  thick  $\text{Gd}_2\text{O}_2\text{S}: \text{Tb}$  phosphor as the x-ray detection material. Unless otherwise specified, the Monte Carlo simulations used Detector 1.

#### Calculation of Scatter to Primary Ratios

The S/P ratio was the total scattered x-ray photon energy absorbed by the detector divided by the total primary x-ray photon energy absorbed by the detector. In the case of Detector 1, all primary and scattered photons incident on the surface cross-sectional detector area were assumed to be completely absorbed by the detector. In the case of Detector 2, the actual energy absorbed by the detector from each incident x-ray photon was computed. Secondary electrons were assumed to deposit their energies at the interaction sites. Energy deposited in the detector from characteristic x-rays emitted following photoelectric interactions was also included. Statistical errors in the resultant S/P ratios were about 1%.

The effect of an air gap on the reduction of the scatter to primary ratio was quantified by a scatter reduction factor,  $f$ , defined as the S/P ratio with no air gap divided by the S/P ratio with an air gap. Since the S/P ratio is reduced as the air gap is increased, the value of  $f$  will generally be greater than 1.

#### I.3. Results

Table I.1 shows the dependence of the S/P ratio on the slot detector width (W) for a 4 cm thick Lucite phantom. The S/P ratio decreased by a factor of  $\sim 2.5$  when W was reduced from 20 mm to 4 mm at all photon energies. Differences in S/P ratios between 20 keV and 30 kV were less than 6%. Figure I.3 (a) and (b) show the S/P ratios as a function

of Lucite phantom thickness (T) for a 4 mm wide slot detector and a 10 mm wide slot detector, respectively. At 20 keV, the S/P ratio ranges from 0.12 to 0.17 for the 4 mm wide slot detector, and between 0.18 to 0.33 for the 10 mm wide slot detector. The S/P ratio decreased by ~10% as the x-ray energy increased from 20 to 25 keV. Average differences in the S/P ratio between 25 and 30 keV were ~3%.

Table I.1. S/P as a function of slot detector width (W) for a 4 cm thick Lucite phantom.

W (mm)	20 keV	25 keV	30 keV	30 kVp
4	0.150	0.132	0.123	0.152
6	0.192	0.184	0.176	0.189
8	0.238	0.215	0.208	0.231
10	0.268	0.239	0.234	0.266
15	0.345	0.302	0.288	0.331
20	0.371	0.352	0.343	0.372

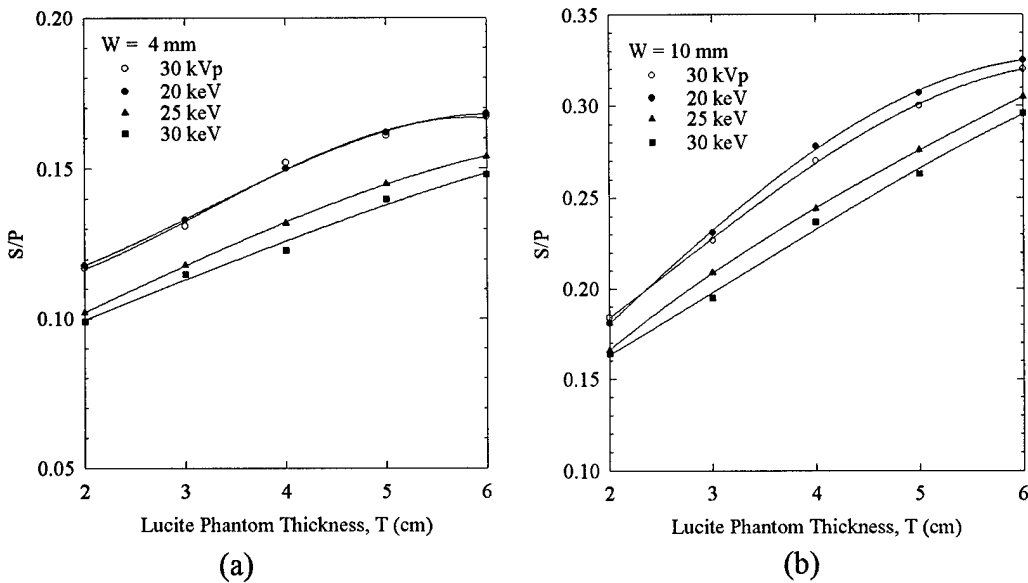


Figure I.3. S/P as a function of Lucite phantom thickness (T) for the (a) 4 mm wide, and (b) 10 mm wide slot x-ray detectors.

Figure I.4 shows the dependence of the S/P ratio on the air gap introduced between the Lucite phantom and a 10 mm wide detector. S/P ratio was reduced by a factor of about two and three using 1.5 cm and 3 cm air gaps, respectively. The S/P ratio was in the range of 0.05 to 0.13 with a 3 cm air gap. Differences in the S/P ratio between 20 keV photons and the 30 kV spectrum were ~3%. Table I.2 gives the resultant values of the scatter reduction factor,  $f$ , as a function of Lucite phantom thickness for the two air gaps at 20 keV. The values of  $f$  were found to decrease with increased Lucite phantom thickness.

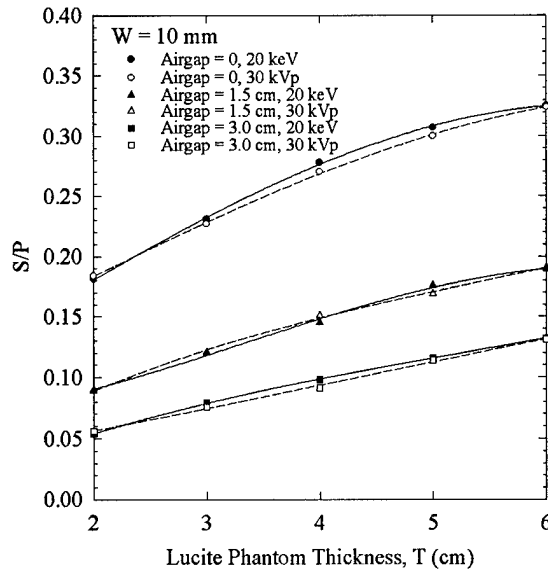


Figure I.4. S/P as a function of Lucite phantom thickness (T) for a 10 mm wide slot detector at Airgap = 0, 1.5, and 3.0 cm. The results are shown in solid and dashed curves for 20 keV and 30 kV x-ray sources, respectively.

Table I.2. Scatter reduction factor,  $f$ , vs. Lucite phantom thickness (T) for two airgaps at 20 keV x-ray energy.

T (cm)	Airgap (cm)	
	1.5	3.0
2	2.01	3.35
3	1.93	2.92
4	1.92	2.84
5	1.74	2.65
6	1.72	2.46

Figure I.5 shows the S/P ratio as a function of x-ray energy for a 4 cm thick Lucite phantom and the effect on the S/P ratio from the introduction of a 3 cm air gap. Also shown in Figure I.5 are the contributions of coherent scatter ( $(S/P)_{Coh}$ ) and Compton scatter ( $(S/P)_{Comp}$ ) to the total scatter. The S/P ratio decreased as x-ray energy increased with a reduction of about 33% between 15 and 50 keV. With no air gap, the  $(S/P)_{Coh}$  ratio was greater than the  $(S/P)_{Comp}$  ratio below about 25 keV. With a 3 cm air gap, however, the contributions from these two scatter processes were equal at an x-ray energy of ~36 keV. The scatter reduction factor,  $f$ , averaged about 2.8 and showed little dependence on the x-ray energy over the range of 15 to 50 keV.

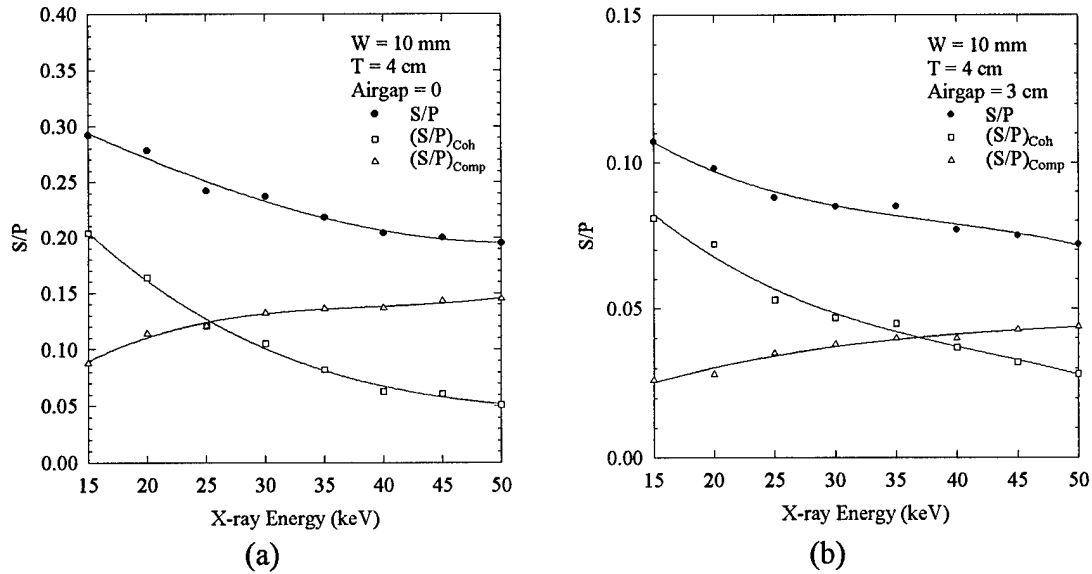


Figure I.5. S/P as a function of x-ray energy for the 4 cm thick Lucite phantom and a 10 mm wide slot detector at (a) Airgap = 0; and (b) Airgap = 3.0 cm.

Figure I.6 shows the effect of the x-ray detector material on the S/P ratios for a 10 mm wide slot detector at 20 keV. The S/P ratio obtained using Detector 2 (i.e., 50  $\mu$ m Gd<sub>2</sub>O<sub>2</sub>S:Tb phosphor), was ~7% higher than that of Detector 1. The introduction of a 3 cm air gap reduced the difference between the S/P ratios obtained with these two detectors to ~ 4%.

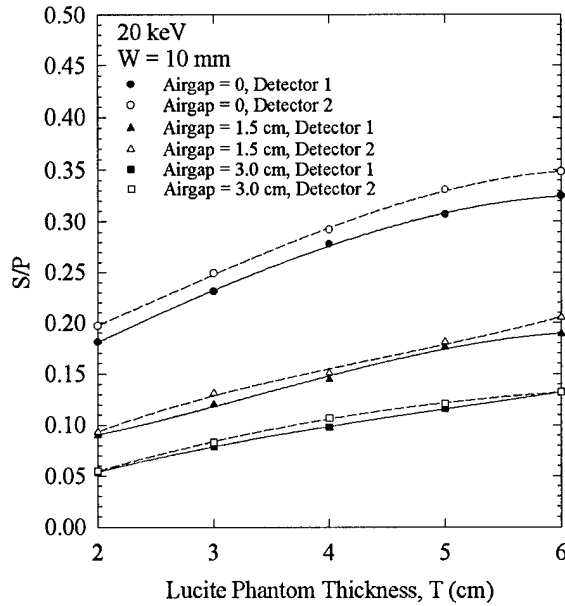


Figure I.6. S/P as a function of Lucite phantom thickness (T) at 20 keV x-ray energy for Detector 1 (i.e., 100% x-ray absorption), plotted in solid lines; and Detector 2 (i.e., a 50  $\mu$ m thick Gd<sub>2</sub>O<sub>2</sub>S:Tb x-ray absorbing

phosphor), plotted in dashed lines. Both detectors are 10 mm wide.

Scattered radiation in mammography was measured using Lucite phantoms by Barnes and Brezovich [1]. One of their experiments was to measure the S/P as a function of x-ray field sizes. We performed simulations for the same field sizes and Lucite phantom thickness. The 30 kVp x-ray spectrum was used in this computation because it was demonstrated in that experiment that S/P values show little dependence on the tube kVp. The computed S/P values were compared to the experimental data measured for a 32 kVp x-ray energy spectrum as shown in Table I.3. For a 3 cm Lucite phantom, the difference between the calculated and measured S/P values is less than 3%. This difference is less than 5% for the 6 cm Lucite phantom. The accuracy in the calculated S/P values shows that scatter radiation can be accurately estimated using Monte Carlo method.

Table I.3. S/P ratios vs. circular x-ray field diameter ( $d$ ) under two Lucite phantom thicknesses (T). The experimental results were taken from the measurements of Barnes and Brezovich [1].

$d$ (cm)	Experimental Results		Present Calculations	
	T = 3 cm	T = 6 cm	T = 3 cm	T = 6 cm
4	0.32	0.54	0.33	0.54
6	0.37	0.65	0.39	0.68
10	0.39	0.80	0.42	0.84
14	0.40	0.86	0.44	0.89

#### I.4. Discussion

In this study, the breast was modeled using a homogeneous block of Lucite, whose molecular form factors are available for Monte Carlo calculations. Lucite is used in many mammographic phantoms including the RMI 156 phantom used for accreditation purposes by the American College of Radiology. Lucite has an effective atomic number (6.5) which is between those of glandular tissue (7.4) and adipose tissue (5.9) [1]. Fahrig *et al* measured the angular distribution of scattered photon energy using a breast equivalent material (BR12) and a 30 kV Tungsten anode x-ray source [13]. This scattered radiation distribution peaked at  $\sim 5^\circ$  which is similar to the distribution of scattered radiation measured from Lucite [20,21]. It is therefore reasonable to take the S/P ratios obtained with a Lucite phantom to be generally applicable to the values expected to occur in clinical mammography.

The S/P ratios for a 4 mm wide slot detector were between 0.10 to 0.17, which are similar to those encountered in conventional screen-film mammography when a 5:1 ratio grid is used [4,6]. Increasing the slot detector width to 10 mm resulted in an increase in the S/P ratio by a factor of  $\sim 1.8$ . The x-ray tube heat loading for a 10 mm wide slot detector is only 40% of that of a 4 mm wide slot detector. Efficient use of the x-rays generated in the x-ray tube would reduce the scan time and thereby minimize patient motion artifacts as well as patient discomfort. In addition, more efficient use of the x-ray beam would enable filters to be used to optimize the shape of the x-ray spectrum to better

match the imaging needs in clinical situations [12,22].

The scatter reduction factor,  $f$ , decreased as the Lucite phantom thickness was increased. This result is expected for the same reason that the observed increase in S/P ratio with phantom thickness is sublinear [23]. The increase in the phantom thickness for a constant (or no) air gap results in an additional layer of material which will contribute proportionally *less* to the scattered radiation in the detector. The reason is that there is an effective air gap (equal to the original phantom thickness) for scattered photons produced in this additional layer of material. Clearly the relative importance of the additional layer will decrease with increasing air gap which is responsible for the decrease of scatter reduction factor with increased phantom thickness as depicted in Table I.2.

In conventional screen-film radiography, scattered radiation is rejected by the use of grids. The radiation exposure to the screen, however, needs to be maintained at a constant level to ensure that the resultant film density is satisfactory. This requires an increase in the x-ray tube output to compensate for any removed scattered and primary x-ray photons, and normally leads to an approximate doubling of the mean glandular dose. Use of a scatter reduction grid with a digital slot detector increased the mean glandular dose by between 30 and 40% as a result of the increased attenuation of the primary x-ray beam [13]. Air gaps can achieve scatter reduction without necessarily increasing the radiation dose and are an attractive option for use in a slot detector geometry particularly since the required air gaps as shown in Figures I.4 and I.5 are much smaller than those normally considered in conventional screen-film mammography [15].

The effect on the patient dose by the use of an air gap with a slot detector geometry will depend on both the characteristics of the detector, and on the manner in which the air gap is introduced. If the detector is quantum noise limited, there will be no need to increase the primary exposure to maintain the same SNR providing the source to detector distance is kept constant. However, if there is a significant electronic noise component from the detector, then an increase in the x-ray tube output would be needed to maintain the same SNR. For a 3 cm air gap introduced by moving the detector away from the patient, the patient dose would increase by about 10% because of the inverse square law fall off in x-ray beam intensity for a source to detector distance of ~60 cm.

For the slot geometry considered in this study, the S/P ratios decreased as the photon energy increased. This differs from the case of mammography performed with large area detectors where the S/P ratios generally shown little dependence on the x-ray energy [1,2]. The reason for this behavior is that in a slot detector geometry, it is only the forward scattered photons which contribute to the S/P ratio whereas in area detectors, photons scattered through large angles will also contribute to the S/P ratio. The relatively constant energy dependence of the S/P ratio for area detectors is a result of the increasing contribution of Compton scattered photons which increase with photon energy (see Figure I.5). Coherent scattered photons are primarily forward scattered and their contribution to the S/P ratio generally decreases with increasing photon energy.

At 20 keV, there are about four times more photons which undergo Compton scattering than coherent scattering in the Lucite phantom. Despite this fact, the contribution of coherent scatter to the S/P ratios is larger than that of Compton scatter at energies below 25 keV as shown in Figure I.5(a). This occurs because the most coherently scattered photons have a small angular divergence whereas the angular distribution of Compton scattered photons is approximately isotropic. This also explains why an air gap is more efficient in rejecting the Compton scattered photons and why the two processes make equal contributions at a higher photon energy (~36 keV) with the 3 cm air gap shown in Figure I.5(b).

X-ray detection materials currently being investigated for scanning slot digital mammography include  $\text{Gd}_2\text{O}_2\text{S:Tb}$  phosphor,  $\text{CsI:Tl}$  crystal, plastic scintillating fiber screens, and hybrid photodiode array. Figure 6 shows that choice of x-ray detection material in a slot detector had very little effect on the resultant S/P ratio. In the case of area detectors, however, the S/P ratios of an ideal screen and a Min-R screen show markedly different responses [2,15]. The reason why a slot detector geometry shows little dependence on the detector material is that most scattered photons reaching the slot detector have directions and energies which are similar to those of the primary photons. This finding suggests that the results obtained in this study will be applicable to any type of detection material providing the geometry is similar to those investigated in this work.

## I.5. Conclusion

At x-ray energies used in mammography, the S/P ratios for a 4 mm wide slot detector ranged from about 0.10 to 0.17, and was comparable to the S/P ratios in screen-film mammography with a 5:1 ratio grid. The S/P ratios for a 10 mm wide slot detector were found to be in the range from about 0.16 to 0.32 but were reduced by a factor of about three by the use of a 3 cm air gap. The ratio of coherent to Compton scattered photons decreased with increasing photon energy and the relative importance of coherent scattering increased with the introduction of an air gap. The detector material used made little difference to the computed S/P ratios with an ideal detector giving results similar to those of a  $\text{Gd}_2\text{O}_2\text{S:Tb}$  phosphor screen. The optimum design for a scanning slot mammography system would likely employ a slot detector width of ~10 mm and use an air gap of ~3 cm.

## I.6. References

1. G. T. Barnes, I. A. Brezovich "The intensity of scattered radiation in mammography," *Radiology* **126**, 243-247 (1978).
2. D. R. Dance and G. J. Day "The computation of scatter in mammography by Monte Carlo methods," *Phys. Med. Biol.*, Vol. **29**, No. 3, 237-247 (1984).
3. M. V. Yester, G. T. Barnes, M. A. King, "Experimental measurements of the scatter reduction obtained in mammography with a scanning multiple slit assembly," *Med. Phys.* **8**, 158-162 (1981).

4. K. L. Junck, A. DeAlmeida, P. Rezentes, X. Wu, G. T. Barnes, "Scatter and grid performance in mammography," Presented at 1996 AAPM annual meeting, Abstract, *Med. Phys.* **23**, 1116 (1996).
5. S. E. Skubic, P. P. Fatouros, "The effect of breast composition on absorbed dose and image contrast," *Med. Phys.* **16**, 544-552 (1989).
6. G. T. Barnes, "Mammography Equipment: Compression, Scatter Control, and Automatic Exposure Control," *Syllabus: A Categorical Course in Physics Technical Aspects of Breast Imaging*. Ed. by A.G. Haus and M.J. Yaffe, RSNA Publications, Oakbrook, IL, 59-68 (1992).
7. L. N. Rothenberg, "Exposures and Doses in Mammography," *Syllabus: A Categorical Course in Physics Technical Aspects of Breast Imaging*. Ed. by A.G. Haus and M.J. Yaffe, RSNA Publications, Oakbrook, IL, 113-119 (1994).
8. M. J. Yaffe, "Direct digital mammography using a scanned-slot CCD imaging system," *Medical Progress through Technology* **19**: 13-21 (1993).
9. E. Toker and M. F. Piccaro, "Design and development of a fiber optic TDI CCD-based slot-scan digital mammography system," *Proc. SPIE* **2009**, 246-252 (1993).
10. Z. Jing, W. Choi, J. K. Walker, W. Huda, "Design of a high resolution digital imaging system for mammography," Presented at 1994 AAPM annual meeting, Abstract, *Med. Phys.* **21**, 875 (1994).
11. J. M. Henry, M. J. Yaffe, Bo Pi, J. Venzon, F. Augustine, and T. O. Tumer, "Solid State X-ray Detectors for Digital Mammography," *Proc. SPIE* **2432**, 392-401 (1995).
12. L. E. Court and R. Speller, "A multiparameter optimization of digital mammography," *Phys. Med. Biol.* **40**, 1841-1861 (1995).
13. R. Fahrig, J. G. Mainprize, N. Robert, A. Rogers, M. J. Yaffe, "Performance of glass fiber antiscatter devices at mammographic energies," *Med. Phys.* **21**, 1277-82 (1994).
14. S. A. Feig, M. J. Yaffe, D. B. Plewes, A. D. A. Maidment, R. A. Jong, "Clinical evaluation of a scanned-slot, full-field digital mammography system," Proceeding of the Third International Workshop on Digital Mammography, June 9-12, 1996, Chicago.
15. A. Krol, D. A. Bassano, C. C. Chamberlain and S. C. Prasad, "Scatter reduction in mammography with an air gap," *Med. Phys.* **23**, 1263-1270 (1996).
16. W. R. Nelson, H. Hirayama, D. W. O. Rogers, *The EGS4 code system*, SLAC-Report-265, Stanford Linear Accelerator Ceneter (1985).
17. Y. Namito, S. Ban and H. Hirayama, "LSCAT: Low-Energy Photon-Scattering Expansion for the EGS4 Code," KEK Internal 95-10, National Laboratory For High Energy Physics, Japan (1995).
18. C. J. Leliveld, J. G. Maas, V. R. Bom, and C. W. E. van Eijk, "Monte Carlo Modeling of Coherent Scattering: Influence of Interference," *IEEE Trans. Nuc. Sc.*, (1995).
19. T. R. Fewell, R. E. Shuping, *Handbook of Mammographic X-ray Spectra*, DHEW Publ. (FDA) 79-8071 (U.S. GPO, Washington, D.C., 1978).
20. E. P. Muntz, T. Fewell, R. Jennings, H. Bernstein, "On the significance of very small angle scattered radiation to radiographic imaging at low energies," *Med. Phys.* **10**, 819-823 (1983).
21. J. Kosanetzky, B. Knoerr, G. Harding, and U. Neitzel, "X-ray diffraction measurements of some plastic materials and body tissues," *Med. Phys.* **14**, 526-532 (1987).

22. R. Fahrig A. D. A. Maidment, and M. J. Yaffe, "Optimization of peak kilovoltage and spectral shape for digital mammography," Proc. SPIE **1651**, 74-83 (1992).
23. P. C. Jones and M. J. Yaffe, "Coherent Scatter in Diagnostic Radiology," Med. Phys. **10**, 40-50 (1983).

## **II. Investigation of Imaging Characteristics of the Plastic Scintillating Fiber Screens**

### **II.1 Introduction**

The primary goal of this research is to design a new plastic scintillating fiber screen (SFS) and optimize its composition for the best possible imaging performance to replace phosphor screen in a scanning slot digital x-ray imaging detector for mammography.

An SFS is composed of individual plastic scintillating fibers fused together with their axes aligned to the direction of the incident x-ray beam. Because the scintillation light dispersion is limited to the individual fiber diameter, a relatively thick SFS can be used to increase its x-ray interaction efficiency without degrading spatial resolution. The scintillation decay time of a plastic scintillator is only a few nanoseconds which guarantees no loss of MTF( $f$ ) when an SFS is used in a scanning detector.

In this project, we investigated the effect of loading high Z elements including tin and lead on the zero spatial frequency detective quantum efficiency, DQE(0), and MTF( $f$ ) of the plastic SFSs. The effects of the SFS thickness and scintillating fiber diameter on the DQE(0) and MTF( $f$ ) were also studied.

### **II.2. Theory**

#### Zero spatial frequency detective quantum efficiency

Noise due to the x-ray conversion processes within an x-ray detector based on the phosphor screens has been characterized by the Swank factor,  $A_S$  [1]. Calculation of  $A_S$  can be performed from the phosphor screen scintillation light output intensity distribution when x-rays of monoenergetic energy incident on the phosphor screen [2,3]. In an SFS, emitted scintillation light is collected and transmitted to the SFS output due to the total reflection principle. The number of light photons exiting the SFS is proportional to the total number,  $N$ , of light photons emitted per absorbed x-ray, and is independent on the depth of x-ray interaction within the SFS. In this study, the emitted light intensity distribution,  $P(N)$ , was therefore used to obtain the Swank factor as given by [2]

$$A_S = \frac{m_1^2}{m_0 m_2}$$

where the  $i$ th moment of  $P(N)$  is defined as

$$m_i = \sum_0^{N_{\max}} P(N) N^i$$

For monoenergetic incident x-ray energy, it has been shown that the zero spatial frequency detective quantum efficiency, DQE(0), of a phosphor screen is given by [2,4]

$$DQE(0) = \eta \cdot A_S$$

where  $\eta$  is the x-ray interaction efficiency, which is the fraction of incident x-rays which interact within the phosphor screen.

### Modulation transfer function

Two stages in the image formation using an SFS determine the screen spatial resolution. First, x-ray interactions with the SFS include Compton scattering, coherent scattering, and photoelectric effect. An incident x-ray undergoes single or multiple interactions before being totally absorbed or scattered out of the SFS. This leads to the spread of incident x-ray energy deposition from the primary interaction site. Second, the emitted light is collected by the scintillating fibers and transmitted to the SFS output. The  $MTF(f)$  of an SFS,  $MTFs(f)$ , is therefore given by

$$MTF_S(f) = MTF_E(f) \cdot MTF_o(f)$$

where,  $MTF_E(f)$  is the spatial resolution of the incident x-ray energy spread. For an SFS made of uniformly packed scintillating fibers of same diameter,  $d$ ,  $MTF_o(f)$  is given by

$$MTF_o(f) = \frac{\sin(\pi \cdot f \cdot d)}{\pi \cdot f \cdot d}$$

### **II.3. Scintillating Fiber Screens**

#### The plastic scintillating fiber screen

A schematic of a slot shaped plastic scintillating fiber screen (SFS) designed for this project is shown in Figure II.1.

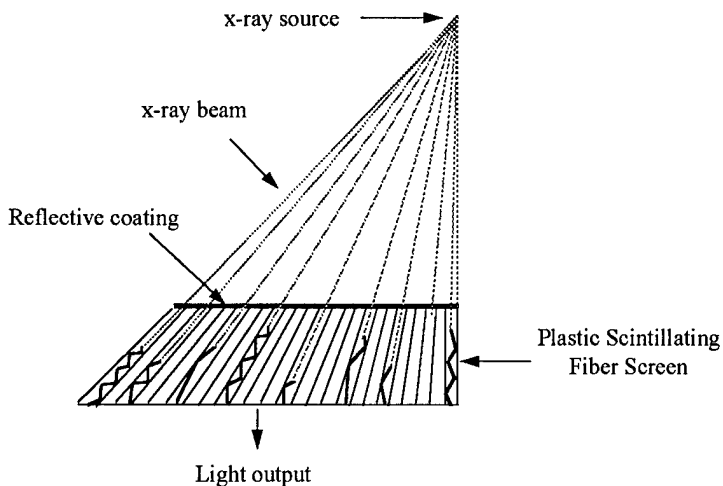


Figure II.1. A slot shaped plastic scintillating fiber screen (SFS).

Because plastic scintillators have much lower x-ray stopping power than phosphor screens used for mammography, it is necessary that the thickness of a plastic SFS should be greater than 1 cm to produce a reasonably high x-ray quantum absorption efficiency. To take account of the parallax effect as a result of this relatively larger thickness, the fiber axes are arranged to be parallel to the direction of the incident x-rays, as shown in Figure II.1. At the end of the slot detector closest to the chest wall, the fibers are normal to the slot plane and vertically below the x-ray focal spot.

A layer of reflective coating which painted on the SFS front surface reflects the light transmitted to this surface back to the SFS output. The measured SFS output increased by a factor of 1.8.

At x-ray energies used in mammography, a large fraction of the x-ray interactions within the plastic SFS is Compton scattering. The majority of the original x-ray photon energy is carried away by the Compton scattered photons. For example, the minimum scattered x-ray photon energy is about 18.55 keV and 26.85 keV for 20 keV and 30 keV incident x-ray photons respectively. The Compton scattered photon can either escape the SFS without interaction (loss of information), or interact again in a remote location within the SFS by photoelectric absorption (register false information).

Adding a small amount of high Z element into the plastic scintillating fiber core material not only improves the SFS x-ray interaction efficiency, but also increases the SFS photoelectric effect cross section. However, addition of the high Z elements in the plastic scintillator also leads to a decreased scintillation light output (or quenching) [5,6]. The choice of a high Z element need to be studied and its concentration shall be optimized.

In this study, the imaging properties of two high Z element loaded SFSs were compared to that of a pure polystyrene (PS) based plastic SFS, SFS:PS. One SFSs contains 10% by weight of tin element in its scintillating fiber core material, SFS:Sn. The other is loaded with 5% by weight of lead, SFS:Pb. The energy conversion efficiency,  $\epsilon$ , of all three SFSs is 4.5%. The fraction,  $q$ , of the scintillation light lost due to quenching is 20% for both high Z element loaded SFSs.<sup>7,8</sup> All three slot shaped SFSs investigated were 2 cm in thickness, 0.8 cm wide and 20 cm long. The diameter,  $d$ , of the scintillating fibers used was 20  $\mu\text{m}$ .

The high Z element which produces better image quality was selected. The SFS was then optimized based on the concentration of this high Z element in the scintillating fiber, the SFS thickness, and the diameter,  $d$ , of the scintillating fibers.

### Scintillation Light Emission

The absorption of x-ray energies causes the excitation of molecules in the scintillating fiber core. The fluorescence processes arise from transitions in the energy level structures of these excited molecules. The energy conversion efficiency,  $\epsilon$ , of a plastic scintillator is defined as the fraction of all incident particle energy which is converted into visible light. One would always prefer this efficiency to be as large as possible. Unfortunately, there are alternate de-excitation processes available to the excited molecules which do not involve the emission of light and in which the excitation is degraded mainly to heat. As a result,  $\epsilon$  of the Polystyrene based plastic scintillators typically low, and is about 3% [7].

In order to use a plastic SFS for mammography, methods to efficiently convert the x-ray energy into scintillation light must be developed. In this project, two solutes were

used: A primary solute and 3-Hydroxyflavone (3HF). Energy transfer between Polystyrene and the primary solute is through a resonant dipole-dipole process, with fluorescence emission peaking at about 340 nm. Energy transfer between the two solutes is through the radiative process in which emission is followed by absorption of light. We have achieved a measured  $\epsilon$  of  $> 4.5\%$  due to the use of the primary solute. The use of 3HF shifts the scintillation light spectrum (peak at 530 nm) to a closer match with the CCD where the CCD quantum efficiency is high. Figure II.2 shows the absorption and fluorescence spectra of 3HF in Polystyrene.

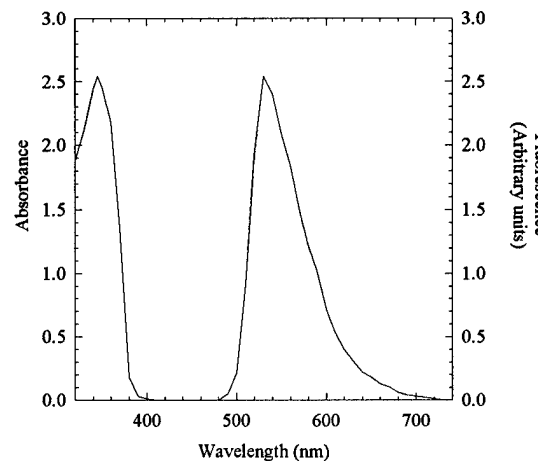


Figure II.2. Absorption and fluorescence spectra of 3HF in polystyrene (PS).

Although Polystyrene based plastic scintillator is transparent to the fluorescence of 3HF, there is some overlap between the optical absorption and emission spectra of the primary solute. This leads to the self-absorption of fluorescence. In this study, a 15% light loss (L) was used to account for this self-absorption.

#### Scintillation Light Collection

Scintillation light produced by the ionizing photoelectron is guided by internal reflections along the fiber, as shown in Figure II.3.

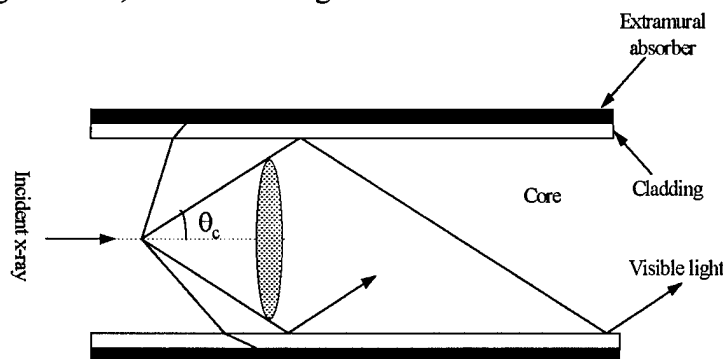


Figure II.3. Transmission of scintillation light within a scintillating fiber

Visible light emitted within the critical angle  $\theta_c$  will be transmitted along each fiber.  $\theta_c$  can be calculated from  $\theta_c = \cos^{-1}(n_{clad}/n_{core})$ . Where  $n_{clad}$  and  $n_{core}$  are the refractive indexes of the optical fiber cladding and core materials. A layer of extramural absorber material is coated to the fiber cladding to absorb those light photons which penetrate the fiber core/cladding interface.

The fraction ( $F$ ) of scintillation light which is transmitted within a fiber in one direction is given by

$$F = \frac{1}{2} \cdot \left(1 - \frac{n_{clad}}{n_{core}}\right) \cdot 100\%$$

The values of  $F$  for some combinations of polymers are given in Table below.

<u>Core Material</u>	<u>Cladding Material</u>	<u>F (%)</u>
Polystyrene (PS) ( $n=1.59$ )	PMMA ( $n=1.49$ )	3.1
PS	Fluorinated Polymer (FP) ( $n=1.35$ )	7.5

The critical angle,  $\theta_c$ , is calculated to be  $31.9^\circ$  for PS/FP fiber, and  $20.4^\circ$  for PS/PMMA fiber. Conventional plastic scintillating fibers use the PS/PMMA core/cladding combination. We have successfully developed PS/FP core/cladding scintillating fibers for this project. This is also a very important step in maximizing the scintillating output from the SFS.

#### II.4. Monte Carlo Simulations

The EGS4 Monte Carlo (MC) code [8] was used. In all simulations, monoenergetic x-rays from a point source were normally incident on the SFS. Three x-ray interaction processes with the SFSs were included: Compton scattering, coherent scattering, and photoelectric effect. Scattered x-rays can either interact again in a remote location within the SFS, or escape without being absorbed. For tin and lead loaded SFSs, characteristic x-rays could be emitted following photoelectric interactions. The Compton recoil electrons, photoelectrons and Auger electrons were assumed to deposit their energies in the x-ray interaction sites.

X-ray interaction efficiency,  $\eta$ , was computed as the ratio of the number of incident x-rays interacted within the SFS to the total number of incident x-rays (history) used for each simulation. The average number,  $N_{exit}$ , of visible photons (2.34 eV) exiting the SFS per incident x-ray was calculated using the equation

$$N_{exit} = E_{ab} \cdot \varepsilon \cdot (1 - L) \cdot (1 - q) \cdot F \cdot 1.8 / 2.34$$

where  $E_{ab}$  (in eV) is the average energy absorption per incident x-ray photon.

In the Swank factor analysis, total x-ray energy deposited,  $E_d$ , from each interacted incident x-ray was generated.  $E_d$  varies due to the variation in the x-ray absorption processes. For each  $E_d$ , the average number of light photons emitted,  $\bar{N}$ , is given by

$$\bar{N} = \varepsilon \cdot (1 - L) \cdot (1 - q) \cdot \frac{E_d}{2.34}$$

We took the wavelength of all emitted light photons to be 530 nm (2.34 eV). The conversion from  $E_d$  to the number,  $N$ , of light photons emitted is also a random process which is described by a Poisson distribution with mean equal to  $\bar{N}$ . In the simulation, for each  $\bar{N}$  computed,  $N$  was generated using the rejection sampling method [9]. The resultant emitted light intensity distribution,  $P(N)$ , was used to calculate the Swank factor.

The point spread functions,  $PSF_E$ , of the spread of x-ray energy deposition were generated for monoenergetic x-ray energies from 15 to 50 keV. The SFS was divided into a two dimensional array composed of squares of  $5 \mu\text{m}^2$  size. Total energy deposition,  $E_{i,j}$ , inside a square centered at  $(x_i, y_j)$  from the normally incident pencil beam of x-rays was calculated. By definition, we have  $PSF_E = E_{i,j}$ . The line spread function,  $LSF_E$ , of this deposited energy spread was calculated by integrating the point spread function in one dimension.  $LSF_E$  is therefore given by

$$LSF_E = \sum_{j=-\infty}^{+\infty} E_{i,j}$$

$MTF_E$  was obtained from the modulus of the Fourier transform of the  $LSF_E$ .

## II.5. Selection of a High Z Element Loaded SFS

### X-ray interaction efficiency

The x-ray interaction efficiency is shown in Figure II.4 as a function of incident x-ray energy for the three SFSs and a Kodak Min-R screen [10]. Loading high Z elements into a plastic SFS significantly improved its x-ray interaction efficiency. X-ray interaction efficiency of SFS:Sn or SFS:Pb was higher than that of the Kodak Min-R screen.

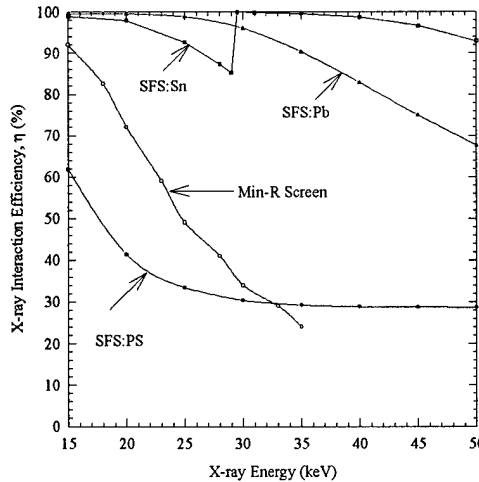


Figure II.4. X-ray interaction efficiency for three SFSs and a Kodak Min-R screen.

### Swank factor

Figures II.5(a) and (b) show the emitted light intensity distributions,  $P(N)$ , for the SFSs at 20 and 50 keV x-ray energies.  $P(N)$ 's of the SFS:PS are always composed of a photopeak and a Compton continuum.  $P(N)$ 's of the high Z element loaded SFSs are dominated by the photopeak. The photopeaks of the high Z element loaded SFSs shift to a smaller  $N$  value than that of the SFS:PS photopeak. This is due to the quenching of scintillation light by the addition of high Z elements in the SFS.

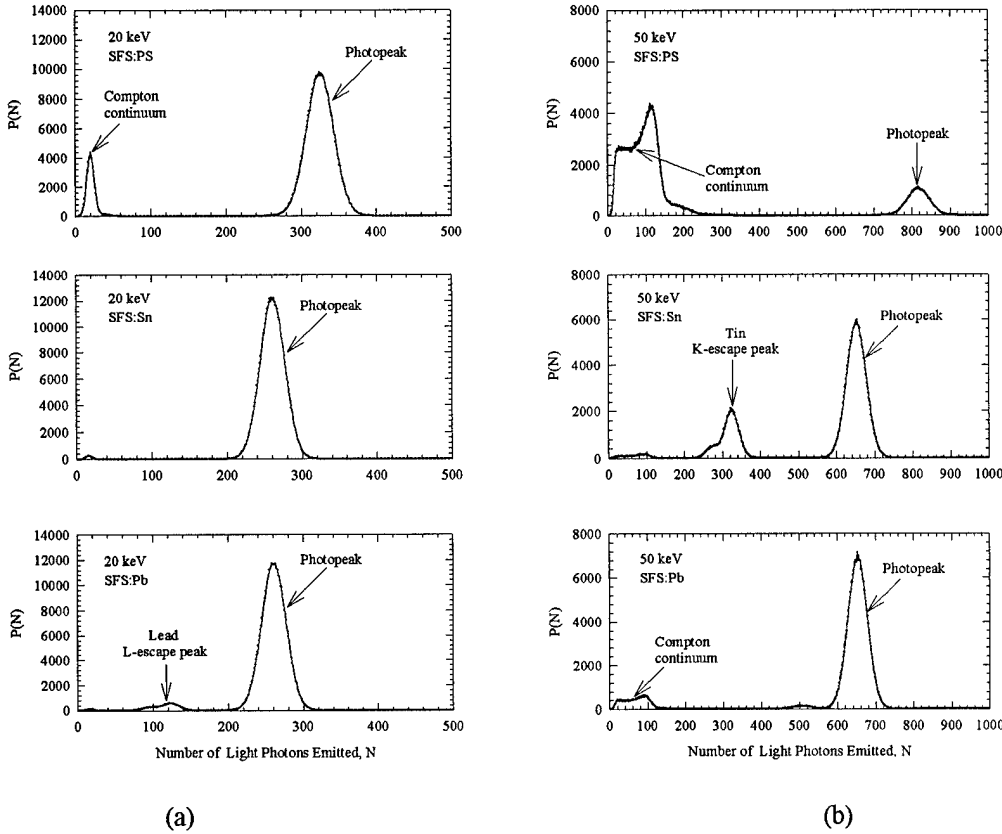


Figure II.5. Emitted light intensity distributions for three SFSs at (a) 20, and (b) 50 keV x-ray energies.

Figure II.6 shows the calculated  $A_S$  of the SFSs as a function of incident x-ray energy. The measured  $A_S$  of an Min-R screen [11] is also shown in Figure 4.  $A_S$  of the SFS:PS decreases quickly as x-ray energy increases which is due to the reduced photoelectric interaction cross section with increasing incident x-ray energy. Because  $P(N)$ 's of SFS:Pb are dominated by the photopeak,  $A_S$  of the SFS:Pb is close to unity from 15 to 50 keV. At x-ray energies below the tin K-edge (29.2 keV),  $A_S$  of the SFS:Sn is also close to unity. Although it drops abruptly just above the tin K-edge,  $A_S$  of SFS:Sn increases as x-ray energy increases further. The results show that Swank factors of both the SFS:Pb and SFS:Sn are significantly higher than that of an Min-R screen.

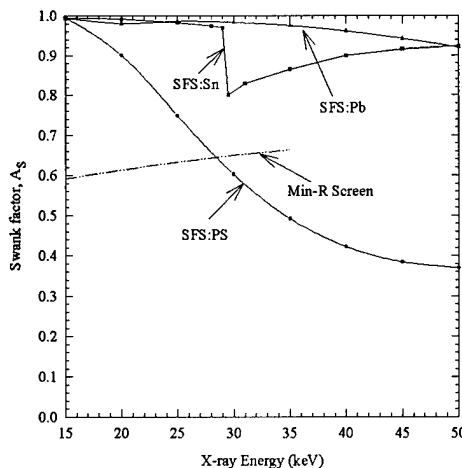


Figure II.6. Swank factor,  $A_S$ , as a function of incident x-ray energy for three SFSs and an Min-R screen.

#### Zero spatial frequency DQE

Figure II.7 shows the DQE(0) as a function of incident x-ray energy for the three SFSs. The DQE(0) of an Min-R screen is also shown in Figure II.7. Loading high Z elements significantly improves the DQE(0) of the plastic SFS. DQE(0) of the SFS:Pb ranges from about 99% to 62% from 15 to 50 keV, and is primarily determined by its x-ray interaction efficiency. DQE(0) of the SFS:Sn is greater than 80%. In the 20 to 30 keV x-ray energy range, DQE(0) of the high Z element loaded SFSs is a factor of three higher than the DQE(0) of the Min-R screen..

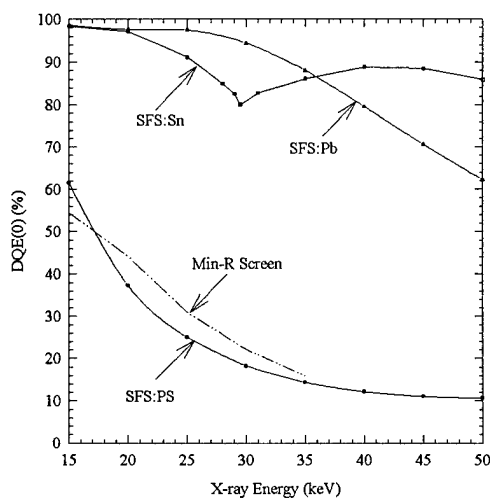


Figure II.7. DQE(0) plotted as a function of incident x-ray energy for three SFSs and an Min-R screen.

### Modulation transfer functions

Figure II.8 shows the  $MTF_0(f)$  for an SFS made of scintillating fibers of 20  $\mu\text{m}$  diameter.  $MTF_0(f)$  values are 0.98, 0.93, 0.85 and 0.75 at 5, 10, 15 and 20 lp/mm, respectively.

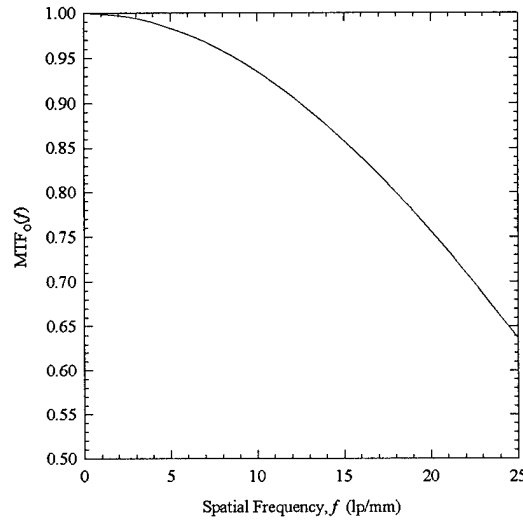


Figure II.8.  $MTF_0(f)$  for an SFS with individual fiber diameter of 20  $\mu\text{m}$ .

Figure II.9 shows the calculated  $LSF_E$  curves at 20, 35, and 50 keV incident x-ray. The major difference in the  $LSF_E$  curves of the three SFSs is shown in the tails of these curves.  $LSF_E$  of the SFS:PS shows little dependence on the incident x-ray energy, and has the smallest spread among the three SFSs. The reason is that scattered x-rays carry most of the incident x-ray energy and has the highest probability to escape in the SFS:PS. For SFS:Pb, the tail in its  $LSF_E$  curve becomes smaller as the x-ray energy increases. This is mainly due to the increased energy transfer to the photoelectrons which deposit their energies at the primary interaction site.  $LSF_E$  of SFS:Sn at 20 keV is better than the  $LSF_E$  of SFS:Pb at all incident x-ray energies. However, the reabsorption of tin K x-rays causes large degradation in the resultant  $LSF_E$  at 35 keV x-ray energy. Similar to the SFS:Pb, the tail in the  $LSF_E$  of the SFS:Sn at 50 keV is smaller than at 35 keV.

It was noted that the assumption of electrons depositing their energies in the x-ray interaction sites is reasonable for Compton recoil electrons (less than 9 keV electron energy) and Auger electrons. However, the energy of the photoelectron increases with increasing x-ray energy at incident x-ray energies greater than the K- or L-edge of the high Z elements. A 15 keV photoelectron from a 20 keV x-ray interaction can travel a distance of about 5  $\mu\text{m}$  before its energy being completely absorbed. Thus, for mammographic x-ray energies, the photoelectron range only has a small effect on the calculated  $LSF_E$  curves shown in Figure II.9.

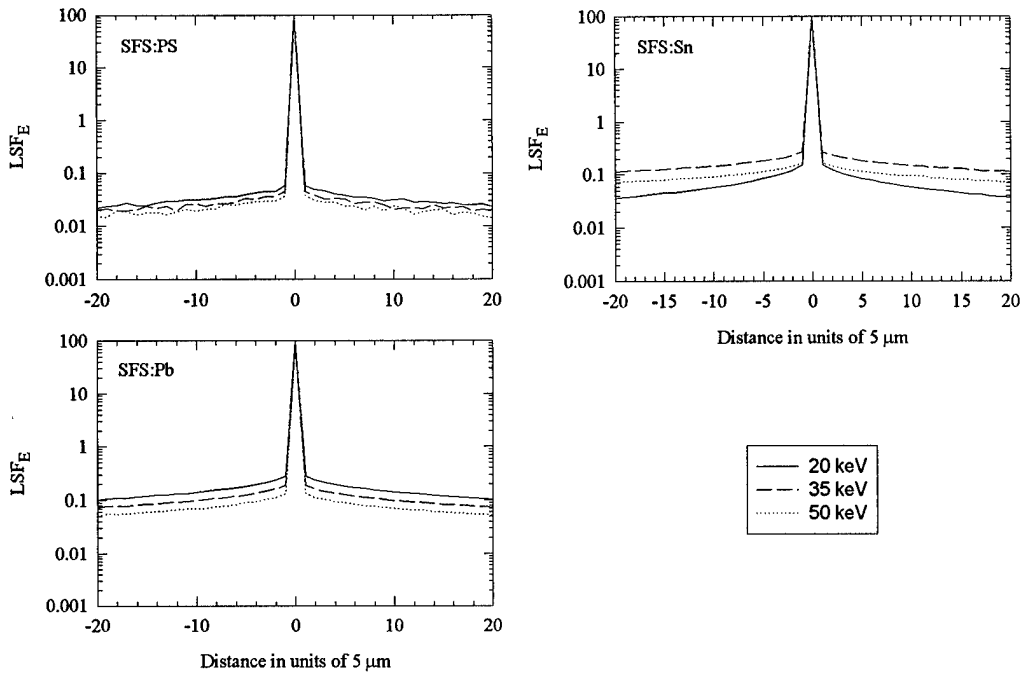


Figure II.9. LSFE curves for three SFSs at 20, 35 and 50 keV incident x-ray energies.

Figure II.10 shows the  $MTFs(f)$  curves of the three SFSs at 20, 35 and 50 keV incident x-ray energies. For each SFS,  $MTFs(f)$  drops quickly in the range from 0 to 2 lp/mm due to the spread of x-ray energy deposition from the primary interaction site. Nevertheless, the  $MTFs(f)$  values of all SFSs remain high (> 50%) beyond 25 lp/mm and are dominated by the 20  $\mu$ m scintillating fiber diameter used.

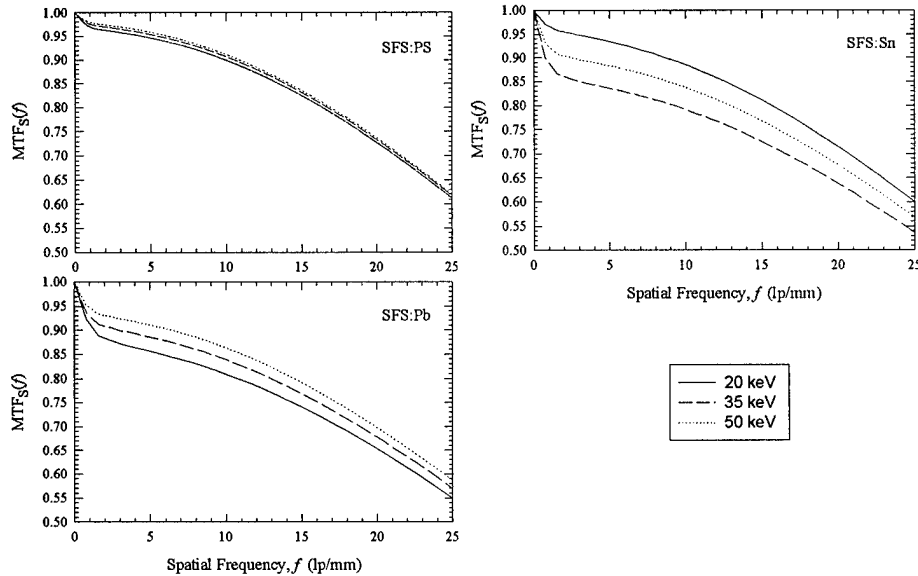


Figure II.10.  $MTFs(f)$  curves of three SFSs made of individual scintillating fibers of 20  $\mu$ m diameter at 20, 35, and 50 keV incident x-ray energies.

Table below summarizes the  $MTF_s(f)$  values of all SFSs at 5, 10, 15 and 20 lp/mm spatial frequencies at 20 keV x-ray energy. However, at x-ray energies significantly higher than the K- or L-edges of the high Z elements, the  $MTF_s(f)$  values were overestimated at high spatial frequency due to the increasing transverse range of the photoelectrons.

$f$ (lp/mm)	$MTF_s(f)$		
	SFS:PS	SFS:Pb	SFS:Sn
5	0.94	0.85	0.93
10	0.90	0.81	0.89
15	0.82	0.74	0.81
20	0.73	0.65	0.72

### Summary

We have investigated theoretically the effect of loading high Z element, lead and tin, on the zero spatial frequency detective quantum efficiency and modulation transfer function of a slot shaped plastic scintillating fiber screen in mammography. Loading high Z elements markedly improved the  $DQE(0)$  of the plastic SFS.  $DQE(0)$  of SFS:Pb is primarily determined by the SFS x-ray interaction efficiency, and is greater than 90% for a 2 cm thick SFS at x-ray energies lower than 30 keV. For SFS:Sn, the  $DQE(0)$  is greater than 80% from 15 to 50 keV. The  $DQE(0)$  of a high Z element loaded SFS was found to be about a factor of three higher than the  $DQE(0)$  of an Min-R screen for mammography. At mammographic x-ray energies,  $MTF(f)$  values of all three SFSs are greater than 50% at 25 lp/mm spatial frequency, and dominated by the 20  $\mu$ m scintillating fiber diameter used in this analysis.

Compared to the 5% by weight of lead loaded SFS, the addition of 10% by weight of tin in the SFS showed less effect on the computed  $MTF(f)$  of the SFSs. Based on this result, we have selected tin as the high Z element to be loaded in an SFS to be used in a scanning slot x-ray detector for mammography.

### **II.6. Optimization of the Tin Loaded Plastic Scintillating Fiber Screens**

#### Optimization of tin concentration in the plastic scintillating fiber

Figure II.11 shows the x-ray interaction efficiency as a function of x-ray energy for three 2 cm thick SFSs with 5%, 7.5%, and 10% by weight of tin loaded into the plastic scintillating fiber core material. As expected, the x-ray interaction efficiency improves with increasing tin concentration at a constant SFS thickness. For the 7.5% by weight tin loaded SFS, its x-ray interaction efficiency is greater than 80% at all x-ray energies encountered in mammography.

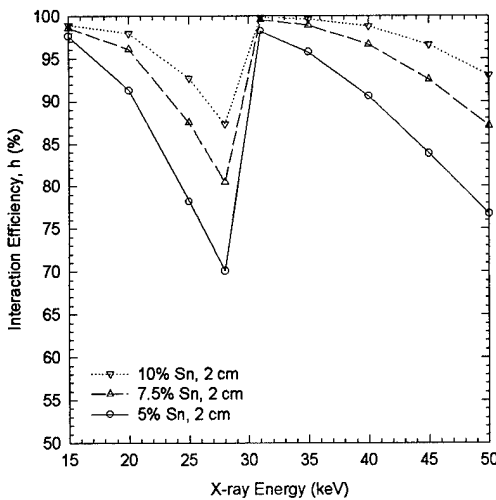


Figure II.11. X-ray interaction efficiency as a function of x-ray energy for three 2 cm thick SFSs with 5%, 7.5%, 10% by weight of tin concentration.

Table below shows the average number of photons output from the above mentioned three SFSs per absorbed x-ray as a function of x-ray energy. Based on our measurement of the tin loaded plastic scintillators, the fraction,  $q$ , of the scintillation light lost due to quenching is assumed to be 10%, 15%, and 20% for 5%, 7.5%, and 10% tin loaded SFSs, respectively. The average number of photons ranges from about 30 to 50 at mammographic x-ray energies, and decreases with increased tin concentration.

Energy (keV)	5% Sn loaded SFS	7.5% Sn loaded SFS	10% Sn loaded SFS
15	30	28	26
20	39	37	35
25	48	46	43
28	52	50	48
35	52	52	50
40	61	61	60
45	69	70	68
50	77	77	76

It is desired that large number of photons to be generated per absorbed x-ray within an SFS to eliminate quantum sink between the SFS and the photon detectors (such as CCD) used to form the final electronic image. We concluded that the addition of 7.5% by weight tin within the SFS is optimized for both x-ray interaction efficiency and x-ray energy conversion efficiency.

The results presented hereinafter are for 7.5% by weight of tin loaded SFSs.

The effect of the SFS thickness on image quality

Figure II.12 shows that the x-ray interaction efficiency increases with increasing SFS thickness. The x-ray interaction efficiency of the 20 mm thick SFS is greater than 80% at x-ray energies below tin K-edge (29.2 keV).

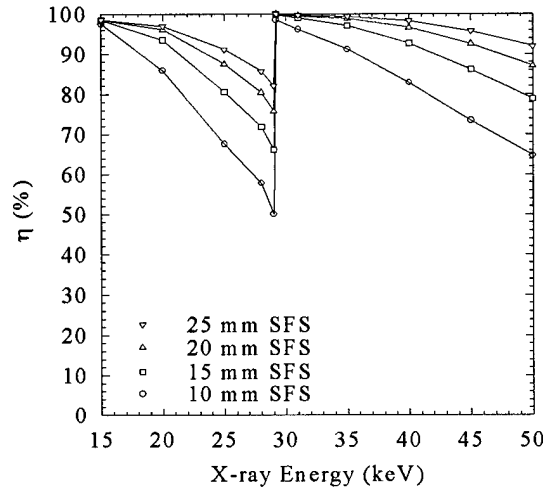


Figure II.12. X-ray interaction efficiency for 7.5% by weight of tin loaded SFSs.

Figure II.13 shows  $N_{exit}$ , the number of visible photons output from the SFS per incident x-ray photon, as a function of x-ray energy.  $N_{exit}$  is generally in the range between 30 and 40 for x-ray energies normally encountered in mammography.

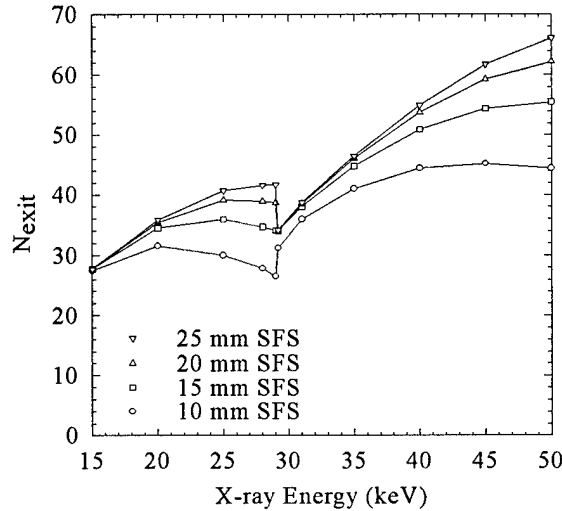


Figure II.13. Number of photons output from 7.5% by weight of tin loaded SFSs.

Figure II.14 shows the Swank factor as a function of incident x-ray energy. The computed Swank factor showed little dependence on the SFS thicknesses investigated.

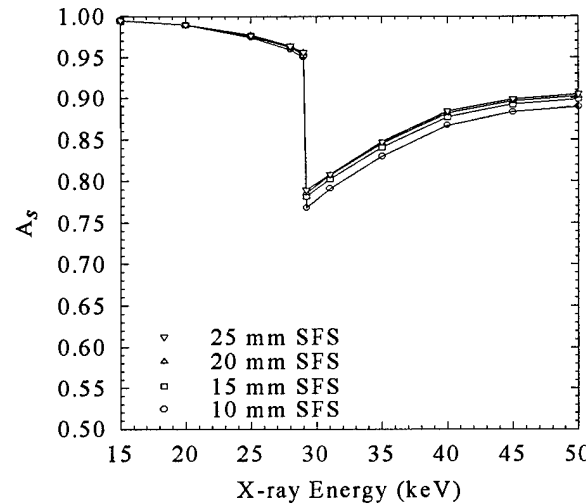


Figure II.14. Swank factors for the 7.5% by weight of tin loaded SFSs.

Figure II.15 shows the DQE(0) as a function of incident x-ray energy. At x-ray energies below tin K-edge, DQE(0) is dominated by the x-ray interaction efficiency. The DQE(0) of the 20 mm thick SFS was > 80% at the photon energies normally encountered in mammography.

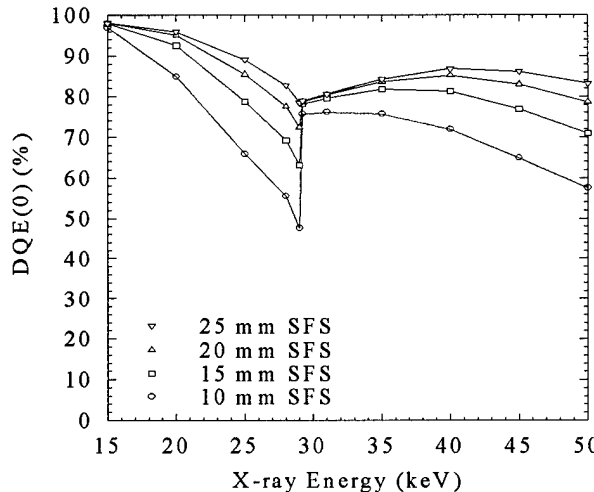


Figure II.15. DQE(0) values for the 7.5% by weight of tin loaded SFSs.

#### The effect of scintillating fiber diameter on image quality

Figure II.16 shows the MTF<sub>s(f)</sub> curves at 20 and 35 keV incident x-ray energies. The MTF<sub>s(f)</sub> values showed negligible dependence on the SFS thickness. The spread of deposited energy from the primary interaction site leads to a drop of MTF values at spatial frequencies less than 2 lp/mm. The reabsorption of tin K x-rays (K edge = 29.2 keV) introduced a further reduction of MTF values at 35 keV. Nevertheless, MTF values were

found to be greater than 60% at 20 lp/mm for the SFS made of 20  $\mu\text{m}$  scintillating fibers at x-ray energies below the tin K edge.

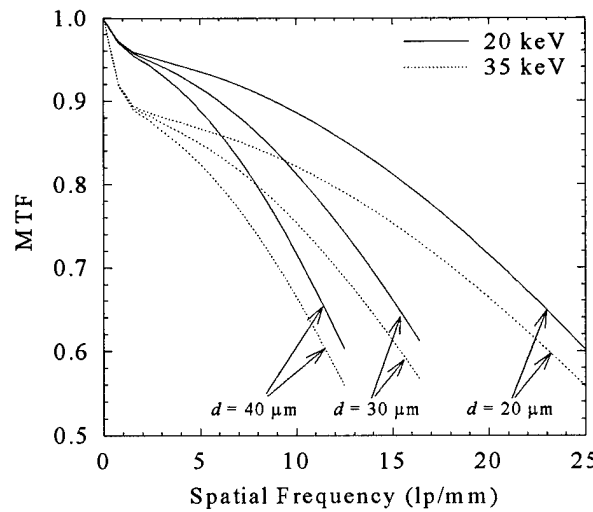


Figure II.16. MTF<sub>S(f)</sub> curves of the 20 mm thick, 7.5% by weight tin loaded SFSs.

### Summary

We found that the addition of 7.5% by weight of tin in the plastic scintillating fiber core material results in both high x-ray interaction and energy conversion efficiency for the SFS to be used in a scanning slot x-ray detector for mammography. Under this condition, DQE(0) values of a 20 mm thick SFS were greater than 80%. MTF(f) values showed negligible variance over SFS thickness from 10 to 25 mm and were found to be greater than 60% for the SFS made of 20  $\mu\text{m}$  scintillating fibers.

Our results show that high DQE(0) and spatial resolution can be achieved with a 20 mm thick SFS composed of 7.5% by weight tin loaded, 20  $\mu\text{m}$  plastic scintillating fibers.

### **II.7. Reference**

1. R. K. Swank, "Absorption and noise in x-ray phosphors," *J. Appl. Phys.* 44, pp. 4199-4203, 1973.
2. R. K. Swank, "Measurement of absorption and noise in an x-ray image intensifier," *J. Appl. Phys.* 45, pp. 3673-3678, 1974.
3. H. P. Chan and K. Doi, "Studies of x-ray energy absorption and quantum noise properties of x-ray screens by use of Monte Carlo simulation," *Med. Phys.* 11(1), pp. 37-46, 1984.
4. C. E. Dick and J. W. Motz, "Image information transfer properties of x-ray fluorescent screens," *Med. Phys.* 8, pp. 337-346, 1981.

5. Sandler and K. C. Tsou, "Quenching of the Scintillation Process in Plastic by Organometallics," *J. Phys. Chem.* 68 (2), pp. 300-304, 1964.
6. W. Wunderly and J. M. Kauffman, "New quench-resistant fluors for liquid scintillation counting," *Appl. Radiat. Isot.* Vol. 41, pp. 809-815, 1990.
7. J. B. Birks, *The theory and Practice of Scintillation Counting*, Pergamon Press, (1964).
8. W. R. Nelson, H. Hirayama, D. W. O. Rogers, *The EGS4 code system*, SLAC-Report-265, Stanford Linear Accelerator Ceneter (1985).
9. J. F. Williamson, "Monte Carlo Simulation of Photon Transport Phenomena: Sampling Techniques," *Monte Carlo Simulation in the Radiological Sciences*, R. L. Morin, pp. 53-101, CRC Press, Boca Raton, 1988
10. Technical Data TI0997 (2-89), Eastman Kodak Company, NY
11. D. P. Trauernicht and R. Van Metter, "Conversion noise measurement for front and back x-ray intensifying screens," *Proc. SPIE* 1231, pp. 262-270, 1990.

### III. Development of A Scanning Slot Digital X-ray Detector for Mammography

#### III.1. Introduction

Figure III.1 shows a scintillating fiber screen based scanning slot digital imaging system designed for mammography. A fan beam of x-rays is formed at the x-ray source, and is always collimated to the slot x-ray detector sensitive area. The slot x-ray detector is mounted rigidly relative to the x-ray tube. To acquire a whole breast image, this fan beam of x-rays and the slot x-ray detector are scanned, in the direction parallel to the chest wall, at about 5 cm/second in a linear motion, a total distance of greater than 20 cm from a position beyond one side of the breast to the other side of the breast. Movement of the x-ray tube plus detector system relative to the compressed breast is under computer control.

The x-ray generator is capable of operating continuously for 4 seconds with uniform output. A W-anode x-ray tube with an 0.3 mm focal spot size and 0.030 mm added molybdenum (Mo) filter will be used. The slot shaped scintillating fiber screen (SFS) is 20 cm long and 0.8 cm wide. The x-ray tube focal spot to slot detector distance is 60 cm.

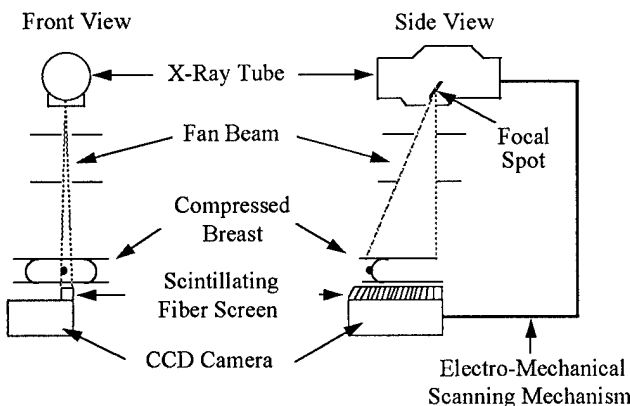


Figure III.1. Schematic of the Scanning Slot Digital Mammography System

#### III.2. A scintillating fiber screen based slot x-ray detector

A schematic of the scintillating fiber screen (SFS) based digital mammography detector is shown in Figure III.2. The 20 cm long, 0.8 cm wide slot shaped detector is formed by eight modules. Each module is composed of a 2 cm thick 7.5% by weight tin loaded SFS, a microfiber image guide with 1:1 input to output ratio, and a front-illuminated 1100 x 330 pixels CCD with 24  $\mu\text{m}$  pixel size. The image guide is composed of the same fibers used to make the SFS, and is actually a continuation of the SFS. The bend in the image guide eliminates the physical interference between the CCDs, and also ensures that the CCDs are not directly exposed to the primary x-ray field.

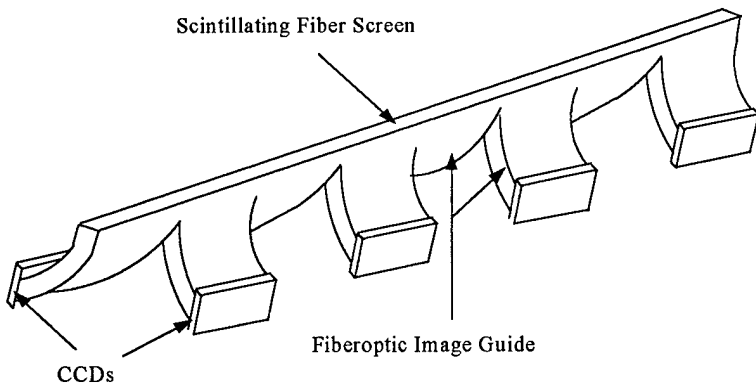


Figure III.2. Schematic of a scintillating fiber screen based slot x-ray detector

A schematic of the slot shaped SFS is shown in Figure III.3. To take account of the parallax effect as a result of this relatively larger thickness, the fiber axes are arranged to be parallel to the direction of the incident x-rays. At the end of the slot detector closest to the chest wall, the fibers are normal to the slot plane and vertically below the x-ray focal spot. A layer of reflective coating which painted on the SFS front surface will reflect the light transmitted to this surface back to the SFS output. The measured SFS output increased by a factor of 1.8.

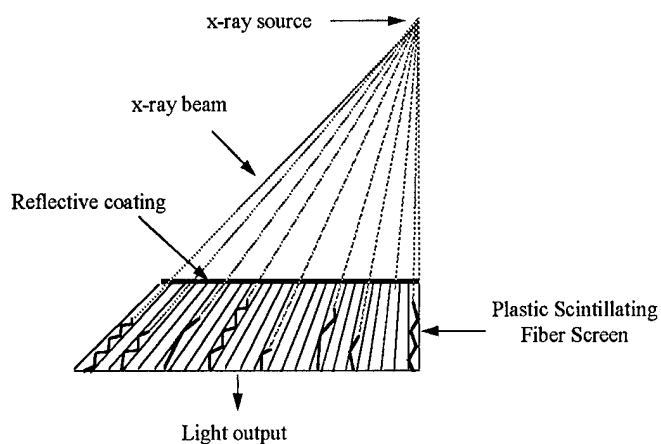


Figure III.3. A parallax corrected plastic scintillating fiber screen (SFS).

The properties of the plastic scintillating fibers designed for this application is shown in the following table.

Fiber diameter	Fiber Core		Fiber Cladding	
	Material	Refractive index	Material	Refractive index
20 $\mu\text{m}$	Polystyrene + 7.5% tin	1.59	Fluorinated Polymer	1.35

Scintillation light produced by the ionizing photoelectron is guided by internal reflections along the fiber. The fraction of scintillation light which is transmitted within the fiber is 7.5%. This is compared to the fraction of 3% for typical plastic optic fibers.

We proposed to use amorphous fluoropolymer AF 1600 as the cladding material which theoretically shall provide a 9% scintillation light collection efficiency. During the progress of this project, we found that properties of Fluorinated Polymer cladding and tin loaded polymer core are matched better than AF 1600 and the tin loaded polymer core. The measured numerical apertures are very close for tin loaded fibers cladded with Fluorinated Polymer and AF 1600. Because Fluorinated Polymer is much cheaper than AF 1600. We decided to use Fluorinated Polymer as the cladding material for fibers used to develop the detector for mammography.

We have mentioned in Section II that the energy conversion efficiency of the Polystyrene based plastic scintillators is typically only about 3%. In this project, two solutes were used to efficiently convert the x-ray energy into scintillation light: A primary solute and 3-Hydroxyflavone (3HF). Energy transfer between Polystyrene and the primary solute is through a resonant dipole-dipole process, with fluorescence emission peaking at about 340 nm. Energy transfer between the two solutes is through the radiative process in which emission is followed by absorption of light. We have achieved a measured energy conversion efficiency of greater than 4.5% due to the use of this primary solute. The use of 3HF shifts the scintillation light spectrum (peak at 530 nm) to a closer match with the CCD where the CCD quantum efficiency is high.

We proposed to load 10% tin by weight into the fiber core to improve the image performance of a plastic SFS. Various weight percentages of Lead (Pb) and Tin (Sn) have been loaded in plastic scintillators for a variety of special applications. However, the commercial metal loaded plastic scintillators are cross linked polymers due to the presence of these metal compounds. It is impossible to draw fibers from these materials because of the cross linking. We have loaded up to 20% by weight of tin element into polystyrene based plastic scintillators. The scintillation light loss due to quenching is measured to be about 15% for the 7.5% by weight of tin loaded plastic scintillator. We also have successfully produced fibers from this material. However, the light transmission within these fibers were significantly reduced. This may be due to the presence of dust in the polymer material, or in the commercial tin compounds used. We are currently investigate the various possible courses which resulted in loss of scintillation light in the fiber.

Although we have produced plastic scintillators with 10% tin by weight, we found from both measurements and simulation (as shown in section II) that loading of 7.5% by weight of tin generates more scintillation light than the loading of 10% by weight of tin in the polystyrene based plastic scintillators. This is the result of two opposite processes: loading tin improves the x-ray energy absorption within the fiber core, but decreases the scintillation light output due to the quenching effect. 7.5% by weight of tin is an optimized loading fraction for this application.

In summary, three key advancements over the current plastic scintillating fiber technology have been made for a plastic scintillating fiber screen to be used in a scanning slot digital x-ray detector for mammography:

- (1) Improved plastic scintillating fiber energy conversion efficiency from ~3% to > 4.5%;
- (2) Increased the scintillation light collection efficiency from 3% to 7.5%;
- (3) Loaded up to 20% by weight of tin into plastic scintillator which remained a thermoplastic from which scintillating fibers were able to be produced..

In addition, a protocol to manufacture parallax corrected SFS module has been developed and tested. Several efforts are being taken to enhance light transmission within the scintillating fiber:

- (1) Improving clean room environment to minimize dust contamination in the fiber core;
- (2) Expanding chemical laboratory to produce clean polymers;
- (3) Investigating new tin compounds which be loaded into the fiber core material.

### III.3. CCD Camera and Readout Electronics

The specifications of the CCDs used (KAF-0360, Eastman Kodak Company) are shown in the table below.

Size	26.4 mm x 7.92 mm
Pixel size	24 $\mu$ m x 24 $\mu$ m
Array	1100 x 330
Full Well Capacity	200,000 electrons
Dark Current @25°C	1080 e <sup>-</sup> /pixel/second
Readout Noise @1 MHz @25°C	50 e <sup>-</sup> rms/pixel (see note)
Amplifier Sensitivity	10 $\mu$ V/e <sup>-</sup>
Quantum Efficiency	average ~40% for the light output from SFP

note: correlated double sampling is assumed

Images will be acquired by scanning a fan x-ray beam and the slot detector in a direction parallel to the short dimension of the detector (7.92 mm, 330 pixels). To allow a smooth mechanical motion, the CCDs are operated in the time-delayed integration (TDI) mode. Each CCD is capable of bi-directional TDI mode operation, and operated in Multi-Pinned-Phasing (MPP) mode of operation to reduce CCD pixel dark current generation.

TDI is based on the concept of taking multiple exposure of the same object. In TDI operation, as the detector is moved across the breast at constant speed the charge collected in each pixel of the CCD is shifted down its column at the same speed as that of the scan but in the opposite direction. This allows the charge generated in one portion of the image to integrate in the detector (CCD) during image acquisition, eventually providing a signal 330 times larger than that accumulated in any individual pixel. The charge packets in each row (1024 out of 1100 pixels) are readout at 2 MHz when they

reaches the last row (the serial register) in the CCD, a line of the final image is then formed. The CCD readout noise only contributes once to the integrated charge signal.

A modular, low noise, fast readout CCD camera has been developed for this project. This CCD camera is designed to be operated at ambient temperature. The output from a CCD is amplified and then digitized at 2 MHz with a 14 bit analog-to-digital converter (ADC) located in the camera head. In our prototype detector, the two CCDs are readout in parallel in order to maintain the 5 cm/second scanning speed. Correlated double sampling (CDS) is implemented to reduce the effect of CCD reset noise. The image data is then captured by a fast image grabber developed by Imaging Technology Inc.. This grabber is capable of acquiring image data at 35 MByte/s, which can handle the simultaneously output from eight of our camera modules.

Fixed pattern noise (FPN) will be removed by a simple algorithm which is being implemented on line during the scanning process in the camera readout hardware. Before image acquisition, two line correction tables (8800 pixels/line) will be recorded first. A dark correction table  $I_d$  is generated by scanning the detector in its normal TDI operation mode for the entire image area without x-ray exposure to the detector. The  $i$ th pixel in the dark correction table is calculated from averaging the pixel intensity over the total pixels in the  $i$ th column along the TDI direction. A flat field correction table  $I_f$  is obtained in the same way with high exposure to the detector so that the x-ray intensity fluctuation is negligible. During image acquisition, each line of the original image  $I_{o,j}$  will be corrected on line by the following algorithm

$$I_{c,j} = F \times \frac{I_{o,j} - I_d}{I_f - I_d}$$

where  $I_{c,j}$  is the  $j$ th line of the corrected image,  $F$  is an arbitrary value. The x-ray quantum noise will not change in the corrected image because the averaging process and high x-ray exposure involved to obtain the correction tables.

#### III.4. A Prototype Testing System

Figure III.4 shows a photograph of a prototype testing system developed for this project. A GE Sonograph 500 t x-ray unit was used with an Mo-anode, 0.3 mm focal spot, and 30  $\mu$ m added Mo filter. A lead collimator was used at the x-ray tube to form a 1 cm wide x-ray beam which cover the whole slot detector area. The focal spot to detector distance was 60 cm. During image acquisition, a testing phantom is moved by a linear motion table in the horizontal direction from one side of the detector to the other side. The testing phantom is mounted on a 5 mm thick acrylic plate, which is supported by the linear motion table. The phantom movement speed is under computer control and can be varied from 1 to 10 cm/second.

Figure III.5 illustrates the functional diagram of this prototype testing system. The synchronization between the phantom movement and CCD pixel charge shift is the critical circuit that permits the TDI mode of imaging operation. A synchronization signal is required once each line to shift the integrating image one pixel in the opposite direction of

the moving phantom. In our experimental setup, an electronic pulse signal which is related to the phantom movement was obtained from the linear encoder attached to the linear table. This signal was modified as the application demands and sent to the CCD camera so that the charge shifting is slaved to the object movement.

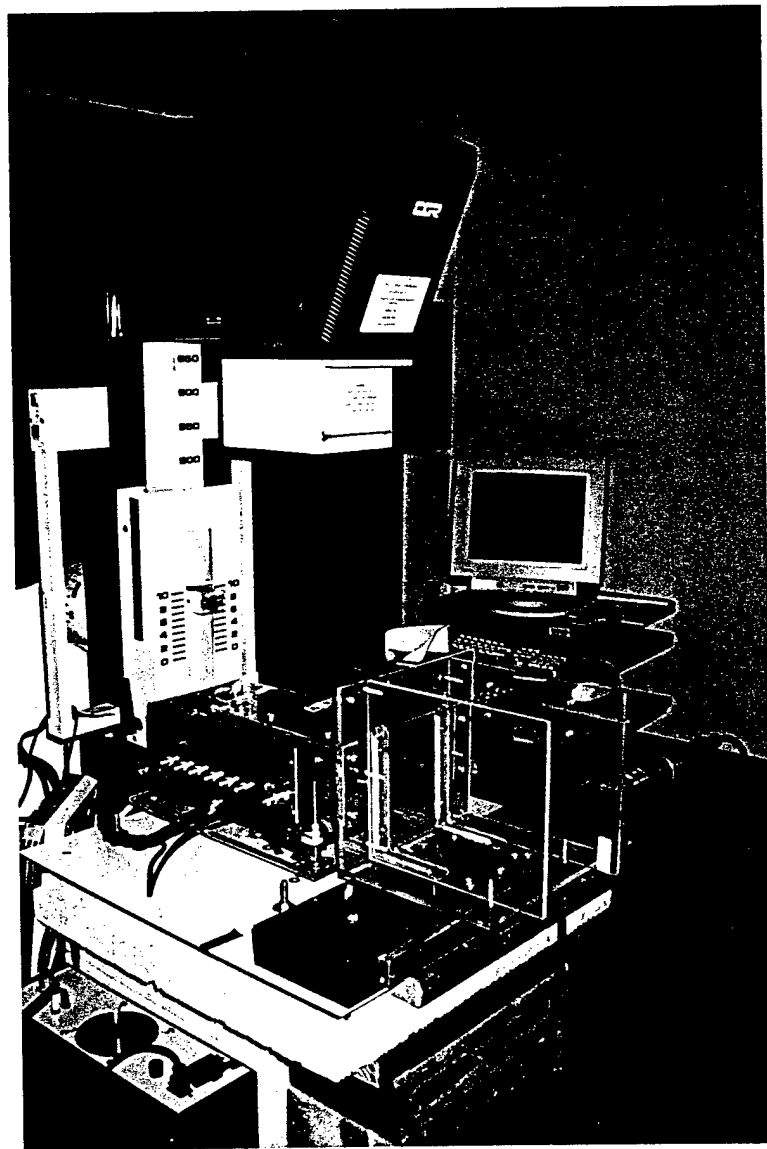


Figure III.4. A photograph of the prototype testing system

The linear encoder has a resolution of  $0.2 \mu\text{m}$ , i.e., the encoder can produce one electronic pulse every  $0.2 \mu\text{m}$  of object travel. The synchronization signal was generated by a timing circuit which counts the number of encoder outputs at an 120 pulses interval ( $24 \mu\text{m}$  linear movement, which is the CCD pixel size). In this way, any speed variation in the object motion is automatically coupled to CCD clocking which moves the charge.

To test this experimental setup, we placed a  $\text{Gd}_2\text{O}_2\text{S}:\text{Tb}$  phosphor (Min-R screen) in optical contact with a CCD through a thin fiberoptical faceplate. X-ray images of a  $1^\circ$  star resolution test pattern (Nuclear Associates, Model No. 07-542) were obtained by scanning the phantom from one side of the detector to another side at 1cm/second speed. The slow speed largely eliminated the afterglow effect of the Min-R screen on the degradation of image resolution. Figure III.6 shows the center of an x-ray image of the star pattern taken using the 0.3 mm focal spot at 28 kVp with detector exposure of  $\sim 10$  mR. The measured limiting resolution from this image is about 14 lp/mm.

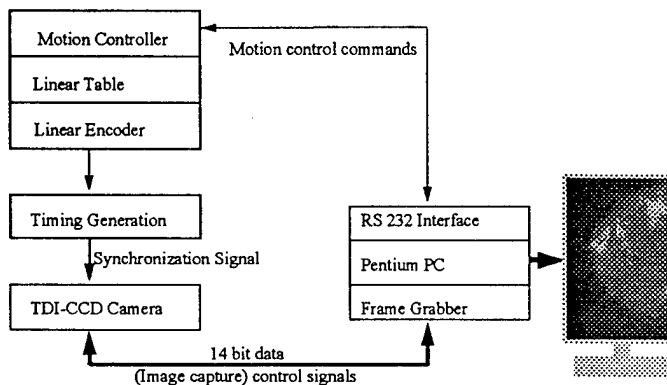


Figure III.5. Functional diagram of the prototype testing system.

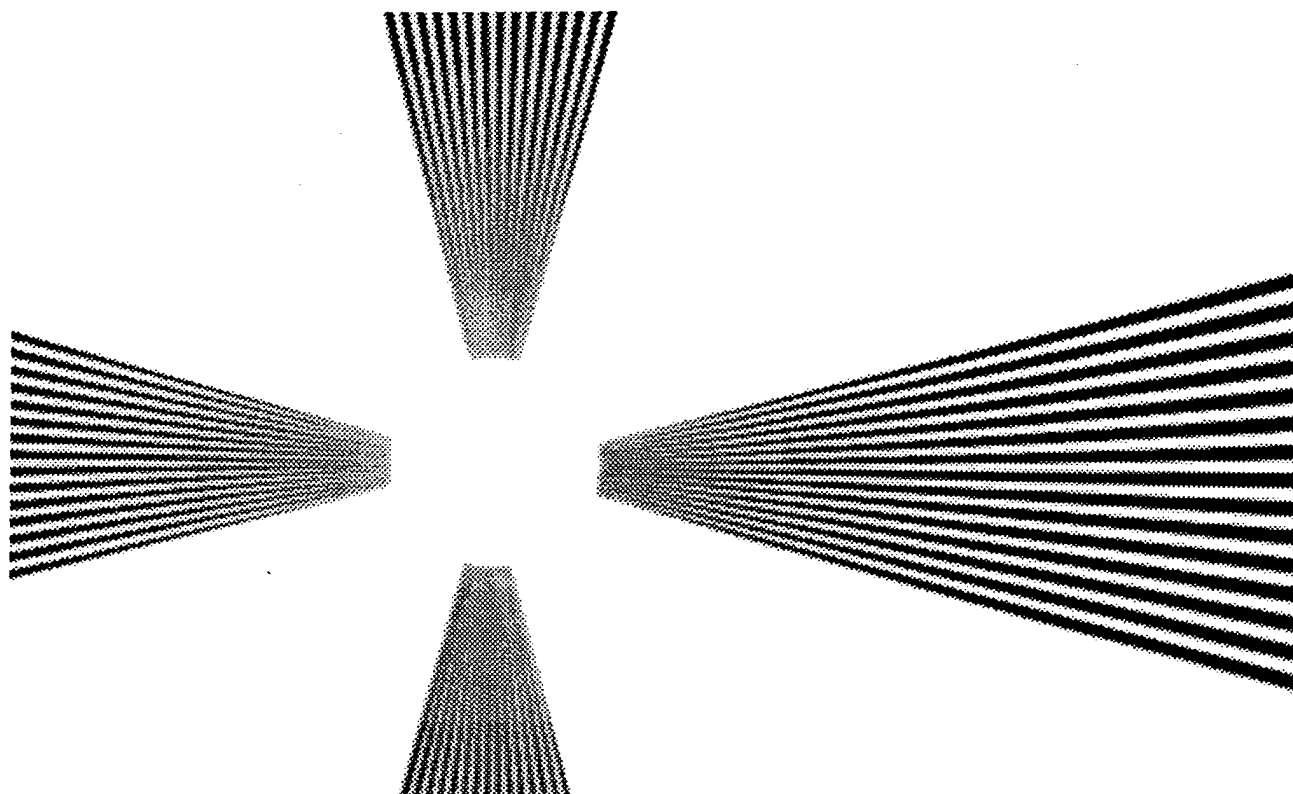


Figure III.6 X-ray image of a  $1^\circ$  star pattern acquired from the prototype slot x-ray detector using a  $\text{Gd}_2\text{O}_2\text{S}:\text{Tb}$  phosphor.

### **III.5. Evaluation of a Prototype CsI:Tl Screen Based Slot X-ray Detector**

#### **The CsI:Tl Screen**

Recently, a new CsI:Tl screen became available from Hamamatsu Photonics K.K., Japan. This screen is composed of prismatic CsI crystals, which is made by using a special evaporation method to enable the needle-shaped CsI crystals (needles) to grow in the direction perpendicular to a supporting base.

A number of properties of this CsI:Tl screen are advantageous for use in a scanning slot x-ray detector for mammography:

- (1) The needle size is  $\sim 5 \mu\text{m}$  and very uniform. When scintillation is generated in each needle, the needle serves as a guide to conduct the light. This fiber-like structure results in a very high resolution.
- (2) The prismatic crystals produce strikingly more efficient light transmission than the powder type material such as  $\text{Gd}_2\text{O}_2\text{S:Tb}$ . This could compensate for its less x-ray energy conversion efficiency (12%) compared to that (15%) of  $\text{Gd}_2\text{O}_2\text{S:Tb}$  screen.
- (3) The scintillation decay time is about  $1 \mu\text{s}$ . This eliminates the problem of afterglow effect related to the use of  $\text{Gd}_2\text{O}_2\text{S:Tb}$  phosphor in the scanning slot detector.
- (4) The light emission peaks at 580 nm and the wavelengths of about 2/3 of the light are greater than 550 nm, where the quantum efficiencies of a front-illuminated CCD are typically high.

Figure III.7 shows the x-ray interaction efficiencies as a function of incident x-ray energy for the 150  $\mu\text{m}$  thick CsI:Tl screen and a Kodak Min-R screen. The x-ray interaction efficiency of the CsI:Tl screen is about 10% higher than the Min-R screen at all x-ray energies used in mammography.

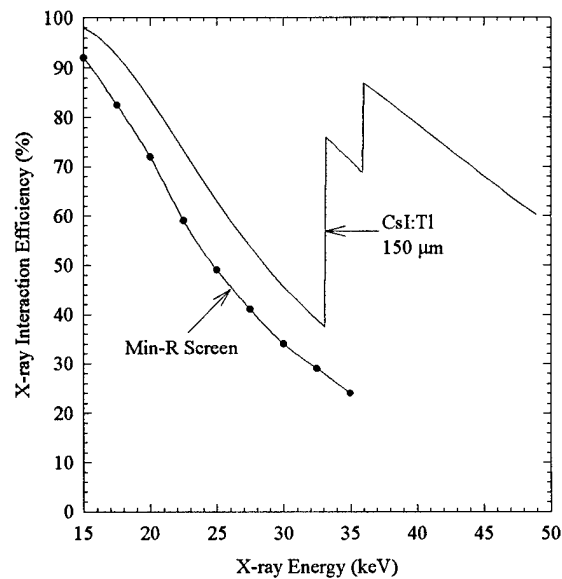


Figure III.7. X-ray interaction efficiency of a 150  $\mu\text{m}$  thick CsI:Tl screen.

Scintillation Light Output and Resolution Measurement

The CsI:Tl screen was tested with the prototype testing system described above. The CsI:Tl screen was optically coupled to one CCD. The signal intensity (pixel values) from x-ray exposure was measured from 24 to 34 kVp. The ratios of the signal intensity from the prototype slot x-ray detectors using the CsI:Tl screen ( $S_{CsI}$ ) vs. using a Min-R screen ( $S_{Min-R}$ ) are summarized in the following table. The results shown the two detectors produced comparable signals at all x-ray energies used in mammography.

kVp	24	26	28	30	32	34
Ratio ( $S_{CsI} / S_{Min-R}$ )	0.92	0.92	0.91	0.92	0.91	0.94

Figure III.8 shows an x-ray image of the 1° star resolution test pattern which was obtained from the prototype slot x-ray detector using the CsI:Tl screen at 4 cm/second scanning speed. The measured limiting resolution from this image is greater than 16 lp/mm. This result shown that the new CsI:Tl screen will provide excellent spatial resolution when used in a scanning slot x-ray detector for mammography.

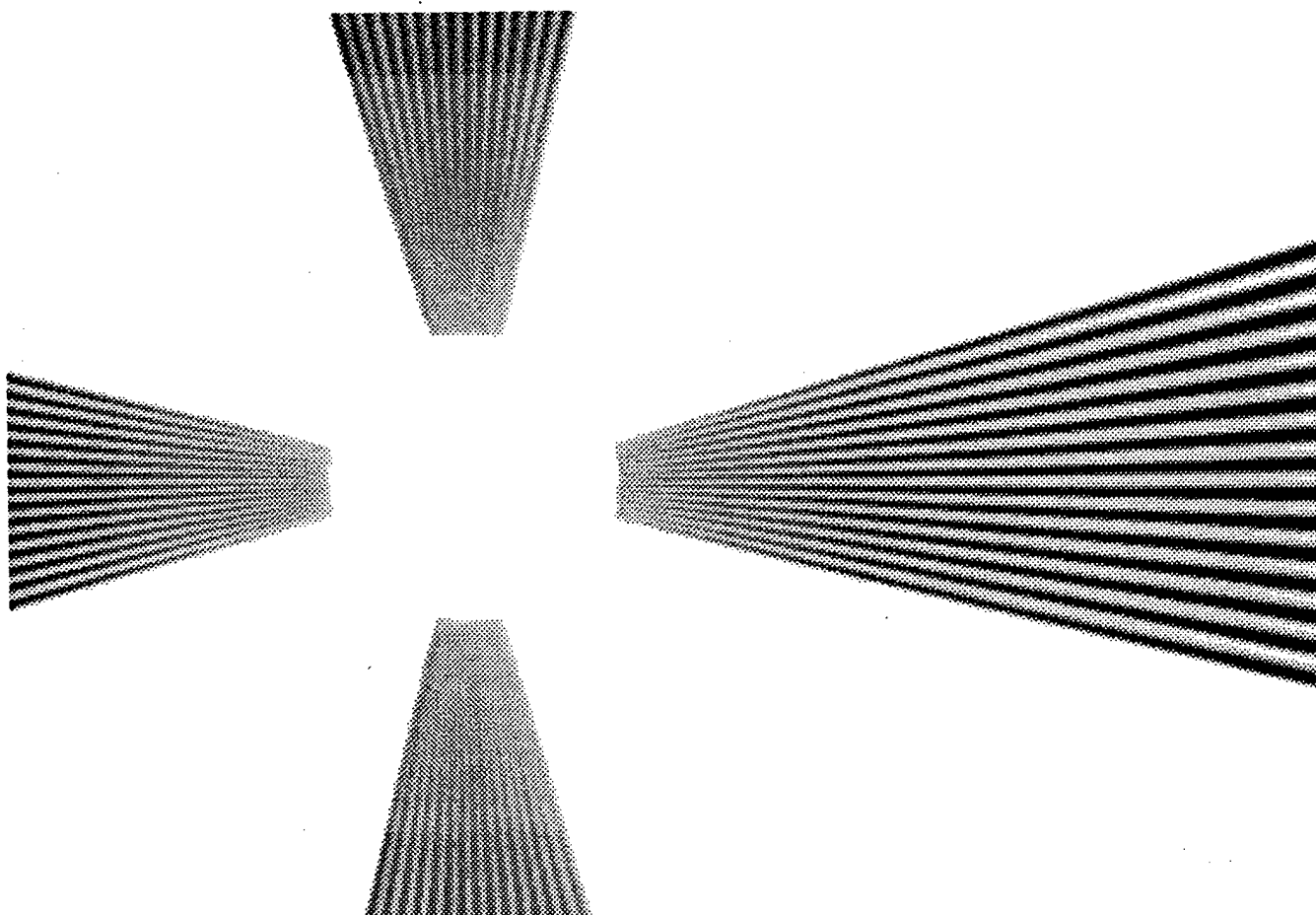


Figure III.8. X-ray image of a 1° star pattern obtained from the prototype slot x-ray detector using a CsI:Tl screen.

### **III.6. A CsI:Tl Screen Based Slot X-ray Detector as an Alternative to the SFS Based Slot X-ray Detector**

To use the CsI:Tl screen in the scanning slot x-ray detector, an image guide made of plastic optical fibers will be developed. This image guide will have exactly the same shape as shown in Figure III.2. The difference is that, for the SFS based slot x-ray detector, the image guide is made of plastic scintillating fibers, and is an extension of the SFS.

The new image guide will be made of clear plastic optical fibers of 10  $\mu\text{m}$  diameter. The fiber has a PMMA/FP core/cladding combination. The numerical aperture (NA) of this fiber is 0.63, which means that it will receive light at less than about 20° incident angle when coupled to the glass fiber optical plate base of the CsI screen. This plastic image guide will be directly bonded to the CCDs. The CCD and associated readout electronics are the same as those used in the SFS based scanning slot x-ray detector. The CCD (KAF-0360) has an average of about 50% quantum efficiency to convert the light from CsI:Tl screen into CCD electrons.

There are two main breakthroughs that can be achieved with this CsI:Tl screen based slot x-ray detector. First, we have shown that the use of this new CsI:Tl screen will provide higher x-ray interaction efficiency, higher MTF, and comparable image signal when compared to a slot detector based on the use of an  $\text{Gd}_2\text{O}_2\text{S}:\text{Tb}$  phosphor (Min-R screen). Second, the use of the inexpensive clear plastic optical fiber image guide will make the cost of this slot x-ray detector very attractive when compared to a slot x-ray detector using the expensive glass fiber optical image guide.

## CONCLUSIONS

The following work elements have been achieved for this predoctoral fellowship research project during the period from August 15, 1994 to December 14, 1996:

- (1) Investigated the effect of the scattered radiation in a scanning slot imaging system using Monte Carlo methods. The results show that sufficient scatter rejection can be achieved using a 3 cm airgap method with negligible dose penalty.

The results of this study can be used to optimize the design of any scanning slot mammography system.

- (2) Studied the potential image quality achievable with plastic scintillating fiber screen (SFS) in mammography applications. The effects of loading High Z element into the SFS on the detective quantum efficiency and spatial resolution were investigated. Choice of a high Z element and its optimal concentration with the SFS were determined.

The results of this study allow the design and development of an optimal SFS to be used in a scanning slot x-ray detector for mammography.

- (3) Made three key advancements over the current plastic scintillating fiber technology: Improved plastic scintillating fiber energy conversion efficiency from ~3% to > 4.5%; Increased the scintillation light collection efficiency from 3% to 7.5%; Loaded up to 20% by weight of tin into plastic scintillator which remained a thermoplastic from which scintillating fibers were able to be produced.

These achievements are critical in realizing the goals of this research. The amount of scintillation light output from SFS determines, to a large extent, the ultimate detector DQE. From the above measurement, we estimate that the detector zero spatial frequency DQE is greater than 70% for typical detector exposure level (> 3 mR) encountered in mammography.

- (4) Set up the testing system to perform the imaging performance measurements. This setup includes a mammography x-ray unit (Senograph 500t), a modified PC based high speed PCI bus frame grabber, and a linear scanning table with a computer controlled motion controller which generates the synchronization signals for CCD camera electronics.

The synchronization between object motion and CCD charge shifting is very important to achieve the goal of 15 lp/mm detector limiting spatial resolution. Also it is critical to align the CCD columns to the scanning direction. In the proposed imaging system, the fast scanning application requires the large amount of digitized image data to be acquired and stored in a very short time. The success in setting up these components allows the prototype SFS detector imaging performance to be evaluated accurately.

(5) Built the CCD camera readout electronics. A circuitry for CCD dark current and detector non-uniformity corrections has been designed and is being integrated into the CCD readout electronics. A measured total thermal and readout noise level of  $75 \text{ e}^- \text{ rms}$  has been achieved at 2 MHz readout rate and  $28^\circ\text{C}$ . The CCD camera and readout electronics are being optimized for lower noise performance at present.

This is another critical component in the prototype scanning slot digital mammography system which determines the detector DQE and the system linear dynamic range. A measured total thermal and readout noise level of  $\sim 75 \text{ e}^- \text{ rms}$  at 2 MHz readout rate and  $25^\circ\text{C}$  has been achieved.

(6) Explored the use of a new CsI:Tl screen as an alternative to the use of an SFS in a scanning slot x-ray detector for mammography. The preliminary results obtained are very encouraging.

The major difficulty of this project is to produce clean  $20 \mu\text{m}$  diameter scintillating fibers with the optimized material composition. The fibers produced so far do not give good scintillation light transmission due to several possible technical problems. As a results, the proposed work as stated in the proposal could not be completed. At this stage, intensive efforts are being taken to produce tin loaded scintillating fibers which will be transparent to its scintillation light.

Thanks to the support by the USAMRMC, the trainee, Zhenxue Jing, has completed his course study, passed his quality exam, and is expecting to obtain his Ph.D. degree by the end of 1996.

## **APPENDIX**

### List of Publications

1. Z. Jing, W. Huda, J. K. Walker, "Image characteristics of plastic scintillating fiber screens for mammography," *Proc. SPIE 2708, Physics of Medical Imaging*, 633-644, 2/1996.
2. Z. Jing, W. Huda, J. K. Walker and W. Choi, "Design considerations of a slot scintillation detector for digital mammography," To be published on the *Proceeding of the Third International Workshop on Digital Mammography*, Chicago, 6/1996.
3. Z. Jing, W. Huda, J. K. Walker, W. Choi, "A scanning slot x-ray imaging detector for digital mammography," Presented at 1996 *AAPM annual meeting*, Philadephial, 1996. Abstract, *Med. Phys.*, Vol. 23, N0. 6, 1996: 1106.
4. Z. Jing, W. Huda, J. K. Walker, "Scattered Radiation in Scanning Slot Mammography," Submitted to *Medical Physics* for publication, July, 1996.
5. Z. Jing, W. Huda, J. K. Walker, W. Choi, "Performance of a CsI:Tl screen based scanning slot detector for digital mammography," Accepted for publication on the SPIE proceeding *Physics of Medical Imaging 1997*, Newport Beach, CA, 2/1997.

### List of Personnel Receiving Pay

Zhenxue Jing  
Medical Physics Program  
Department of Nuclear & Radiological Engineering  
University of Florida  
Gainesville, Fl32611